TECHNICAL MEMO

Date: August 10, 2026

To: PFC Documentation Set

From: David Potyondy

Re: Rock-Cutting Support for PFC [rcPkg9.1]

Ref: unnumbered

This memo describes support for modeling rock cutting with PFC. The capability is provided in the rock-cutting package (**`rcPkg9.N`**) that works with PFC2D version 9 (where **`N`** is the package version number). The rock-cutting package is built upon the material modeling support package (Potyondy, 2025). This memo updates Potyondy (2019a) to work with PFC2D version 9.

The rock-cutting package supports creation and testing of a synthetic rock. The tests include standard rock-mechanics tests (direct tension and compression) and a rock-cutting test. The rock-cutting test supports both dry and wet cutting, during which up to two cutters are moved across the surface of the synthetic rock, while monitoring forces on the cutters, damage in the rock, and all energy quantities of the cutter-rock system. Wet cutting is modeled by applying a confining pressure to the evolving rock surface via the chaining algorithm. The chaining algorithm repeatedly identifies a connected chain of particles on the rock surface and applies an external force to each of these particles based on the local chain geometry and specified pressure.

The rock-cutting package is described in the first major section, which includes a description of wet cutting. Rock-cutting examples are given in the second major section. The first example serves as a base case to demonstrate system behavior during dry cutting under conditions of the SiPlan Base Case test. The rock is Torrey Buff sandstone, with a 200-mm grain size, which is sufficient to resolve the cutter chamfer, and a sample size sufficient to reach a steady-state condition. The second example performs both dry and wet cutting on the material with a grain size equal to that of Torrey Buff sandstone, with wet-cutting pressures of 1 and 5 MPa. The second example exercises the chaining algorithm to confirm that it is behaving in a robust and reasonable manner and provides a comparison of dry and wet cutting. It is demonstrated that the damage process during dry cutting is brittle, whereas the damage process during wet cutting is ductile.

TABLE OF CONTENTS

Table of Contents i
1.0 ROCK-CUTTING PACKAGE 1
1.1 Cutting-Test Model 2
1.2 System-Behavior Quantities 8
1.3 Wet Cutting 13
2.0 SYNTHETIC MATERIAL 23
2.1 Material Genesis 23
2.2 Parallel-Bonded Material Parameters 25
2.3 Material Microproperties 29
2.4 Material Response (Lab and Cutting Tests) 31
2.4.1 Lab Tests 31
2.4.2 Cutting Tests 33
2.4.3 Cutting Tests with Version 6 38
3.0 REFERENCES 56

1.0 ROCK-CUTTING PACKAGE

The rock-cutting package supports creation of a 2D bonded-particle material, standard laboratory testing (direct tension and compression) of the material, and rock-cut testing of the material. The material creation and standard laboratory testing capabilities are described in Potyondy (2025), and the rock-cut testing capability is described in this memo.

The primary mechanisms believed to be controlling the behavior of the cutter-rock system are described in Potyondy and Blanksma (2015). During a physical rock-cut test, a cylindrical cutter (with a chamfer around the cutting face) is moved across the rock surface, while keeping the back-rack angle, depth of cut, and velocity fixed. The physical test may be either a Vertical Turret Lathe (VTL) test or a SiPlan test. The VTL test is performed upon a rotating cylindrical rock specimen, and the SiPlan test is performed upon a fixed rectangular cuboid rock specimen. The cutter is moved slowly inward during the VTL test to produce a spiral groove, and the cutter is moved parallel with the rock surface during the SiPlan test to produce a straight groove.

The conditions of a physical rock-cut test can be replicated directly with a 3D cutting model but must be approximated with a 2D cutting model (see Figure 1). The rock and cutter in the 3D model consist of spherical particles and faceted walls, whereas the rock and cutter in the 2D model consist of unit-thickness disks and a unit-thickness segmented wall. The synthetic cutter in the 2D model is not a cylinder, instead being a unit-thickness chamfered edge. The 2D synthetic cutter is not cutting a groove, instead cutting a slice completely across the unit-thickness rock specimen. It is expected that the cutting forces in the 2D model will not match the cutting forces in physical rock-cut tests, and that matching these forces will require a 3D cutting model (Ledgerwood, 2012, 2013; LeBaron et al., 2024).[1]

[1] A. LeBaron (personal communication, July 14, 2026) is modeling rock cutting successfully using the PFC3D flat-jointed material and shining-lamp algorithm as he states in the following. *Interest in rock cutting with PFC3D has been growing in SLB. We're up to 2 PFC licenses, 2 dedicated machines to run models, and trying to find another engineer to train as demand for my work has been steadily increasing. I've done many studies of cutter shapes, including some work analyzing/optimizing the Serra Blade cutting element. I credit the flat joint model for a lot of the success. It seems to capture the ductile-brittle transition in rock cutting, creating larger rock chips and lower specific energy at higher depths of cut. I also have indications that it matches fracture toughness for at least 2 rock types via laboratory rock chipping tests (not by any formal fracture toughness tests). // The shining-lamp algorithm has been up and running for about a year now, including a couple recent tweaks to simulate the presence of a pressurized, fluid-filled crack inside the rock in conjunction with the smooth joint model. Lab testing is in progress to judge how accurate the method is and optimize the smooth-joint parameters. // That's all for now. Staying busy for sure—running models in PFC3D and adding features to our simulation environment is pretty much all I do these days*.

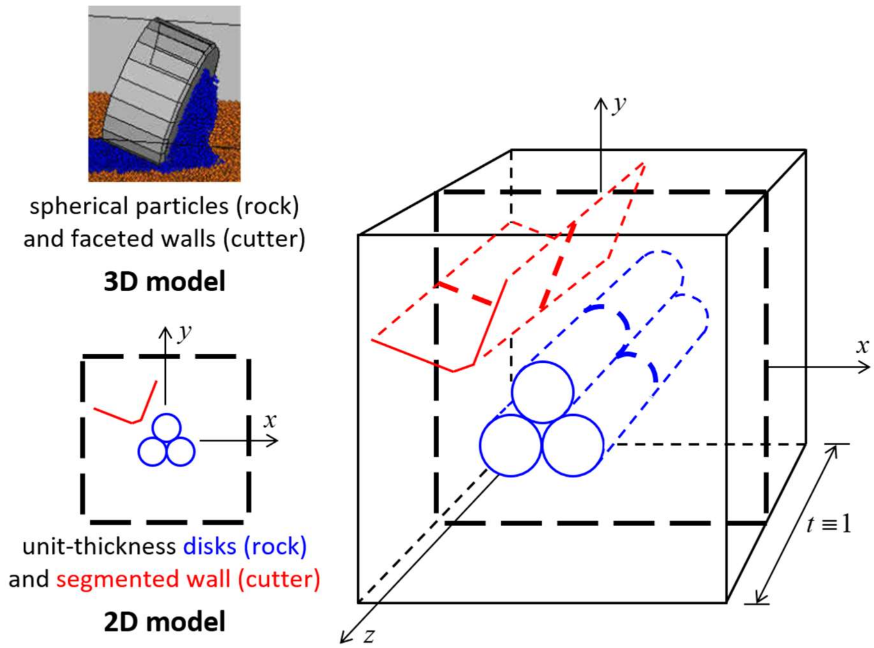

Figure 1 ***The 2D cutting model consists of unit-thickness disks (rock, blue) and a unit-thickness segmented wall (cutter, red) centered in the xy plane. The 3D cutting model is shown in the upper-left inset.*** (From Fig. 4 of Ledgerwood [2013])

1.1 Cutting-Test Model

Cutting tests are performed upon specimens that have been created within the material vessel. The cutting-test parameters are listed in Tables 1 and 2. The modeled system is shown in Figure 2. The rectangular cuboid rock specimen of height (H) and width (W) is gripped on the bottom and right sides, while one or two cutters (n_c) are moved across the rock surface. The grip grains are identified via grip thickness (t_g), and the grip grains are not allowed to translate or spin during the test.[2] The geometry of each cutter consists of an ordered list of n_f linear facets. The facet vertices $(\mathbf{c}_i)$ are expressed in a local $x'y'$ coordinate system, with the origin of the local system serving as a reference point to orient and position the cutter with respect to the upper-left corner of the rock specimen. The cutter is rotated clockwise by the back-rack angle (θ_r) and positioned at a depth of cut (D) with an initial specimen offset (o_c). The cutter reference point should be the point on the initially positioned cutter that is farthest below the rock surface. The 3D area of cut $(A_c)_{3D}$ is used to compute the mechanical specific energy. The cutter is moved parallel with the rock surface at a velocity (V). If the desired system behavior is not quasi-static, then the local-

[2] For the wet-cutting tests, the chain balls correspond with the grip grains, and because these grains are not allowed to move, the pressure does not load the rock in this region.

damping factor (α_c) should be set to a small value.[3] The material behavior at the cutter-rock interface[4] is controlled by the cutter-rock effective modulus, stiffness ratio, and friction coefficient $(E_c^*, \kappa_c^*, \mu_c)$.

Wet cutting is modeled by applying a confining pressure (P) to the evolving rock surface via the chaining algorithm. The chaining algorithm is summarized here and is described in detail by the text associated with Figures 6–15. The chaining algorithm repeatedly identifies a connected chain of particles on the rock surface and applies an external force to each of these particles based on the local chain geometry and specified pressure. The chain consists of an ordered list of balls joined by existing contacts and within a specified gap (g) of one another. If chain seals are activated, then a seal is formed at each cutter-rock interface such that pressure cannot penetrate. The seal extends from the first to last balls in compressive contact with each cutter, and the back-face facet is excluded from consideration (unless $f_b = 0$). Pressure is not applied to the chain segments between sealed balls. The chain-regeneration interval (N_c) specifies how often the chain is built. Building the chain also applies the confining pressure. During the model set-up phase, the chain is built, and the model is brought to static equilibrium (determined by $\varepsilon_{\lim}$ and $n_{\lim}$).

The following model control and monitoring parameters can be specified.

- Horizontal layers (of thickness t_l) can be defined to visualize the deformation field. The model can be run in deterministic mode $(M_d = \text{true})$ to ensure that results are repeatable; computational speed can be increased by setting deterministic mode to false — see the **model deterministic** command. The sampling intervals for the history and energy quantities are specified via R_h and R_E, respectively.
- The cutter-rock system is surrounded by a vacuum box. As the cutter moves across the rock surface, grain fragments may form and be ejected from the surface. The lack of a gravity field means that these fragments will continue to move in their initial direction, and their presence will no longer affect the behavior of the cutter-rock system. To increase computational speed, any grain that moves outside of the

[3] A local-damping factor of 0.7 corresponds with heavy damping, which should be used when it is desired to maintain quasi-static conditions during the test. If dynamic effects are being studied (e.g., the effect of cutter velocity upon system behavior), then the factor should be set to a small (see the footnote associated with Table 2 in Section 3.4 of Potyondy and Blanksma [2015]). Contact dashpots or Maxwell damping (Itasca, 2026b) are more appropriate than local damping for dynamic modeling and both schemes should be considered when modeling dynamic effects. Maxwell damping is in FLAC2D, FLAC3D, and 3DEC, and it could be added to PFC2D and PFC3D.
If Maxwell damping is available in PFC2D then it or Maxwell damping should be

[4] The linear contact model is installed at the cutter-rock contacts. Cutter-rock contact stiffness is set based on the effective modulus and stiffness ratio, and cutter-rock friction coefficient is set equal to the friction coefficient.

vacuum box is deleted and thereby removed from the model. The vacuum box encloses the initial cutter-rock system, with a width of 1.1 times the initial system width, a bottom just below the specimen bottom, and a top defined by the vacuum box top offset (o_v). The update interval for the vacuum process is specified via R_v.

- The material microstructure can be displayed via microstructural plot sets (Potyondy [2025, section Microstructural Plot Sets]). The microstructure is shown only in the microstructural box (with center $\mathbf{x}_b$ and dimensions $\mathbf{d}_b$). The update interval for microstructural plot set monitoring is specified via R_{ps}.[5]
- Cracks that form during the cutting test are stored and displayed by the crack-monitoring package (Potyondy [2025, section Crack Monitoring]). A crack has geometric information that includes size, position, normal direction, and gap. The size is set at creation and then frozen. The position, normal direction, and gap are updated to correspond with material motion after bond breakage. If one or both parent grains have been deleted, the crack is denoted as an orphan, and its position is frozen. Either all cracks, or only the non-orphan cracks between nearby grains with a gap less than the crack-filtering gap (g_f), can be displayed. The update interval for crack monitoring is specified via R_c.[6]

Table 1 Cutting-Test Parameters (1 of 2)

Parameter	Type	Range	Default	Description
Cutting-test properties are listed via **`rcListProps`**.				
N_t, **`rc_testName`**	STR	NA	no name	test name (for plot headers)
Geometry, position, and orientation group				
n_c, **`rc_cutterNum`**	INT	$\{1,2\}$	1	number of cutters
$n_f^{(c)}$, **`rc_facNum(`**n_c**`)`**	INT	$[1,\infty)$	NA	number of cutter facets, cutter (c)
$(\mathbf{c}_i')^{(c)}$, **`rc_facPt(`**$n_f^{(c)}$**`)`**	VEC2	$[\mathbb{R},\mathbb{R}]$	NA	cutter-facet vertices, cutter (c) (local system, $i=\{1,2,\ldots,n_f^{(c)}+1\}$)
$\theta_r^{(c)}$, **`rc_rakeAng(`**n_c**`)`**	FLT	$[0.0,90.0)$	0.0	back-rake angle, cutter (c) [degrees]
$D^{(c)}$, **`rc_DOC(`**n_c**`)`**	FLT	$(0.0,\infty)$	NA	depth of cut, cutter (c) (from rock surface)

[5] A large value will decrease runtime, and saved models will have updated plot sets, because they are updated during the save process. A small value is required to observe the microstructure during a run.
[6] A large value will decrease runtime, and saved models will have updated crack geometry, because the crack geometry is updated during the save process. A small value is required to observe crack locations during a run.

$o_c^{(c)}$, **rc_offSet(** n_c **)**	FLT	$[0.0,\infty)$	0.0	cutter offset, cutter (c) (from left side of specimen)
$(A_c)_{3D}^{(c)}$, **rc_Ac3D(** n_c **)**	FLT	$(0.0,\infty)$	NA	3D area of cut, cutter (c) (see Eq. (8))
Boundary and initial conditions group				
t_g, **rc_tg**	FLT	$(0.0,\infty)$	$0.1H$	grip thickness (material-vessel height: H)
α_c, **rc_localDampFac**	FLT	$[0.0,0.7]$	0.0	local-damping factor
$V^{(c)}$, **rc_vel(** n_c **)**	FLT	$(0.0,\infty)$	NA	cutter horizontal velocity, cutter (c)
Material properties group				
$(E_c^*)^{(c)}$, **rc_emod(** n_c **)**	FLT	$[0.0,\infty)$	0.0	cutter-rock effective modulus, cutter (c)
$(\kappa_c^*)^{(c)}$, **rc_krat(** n_c **)**	FLT	$[0.0,\infty)$	0.0	cutter-rock stiffness ratio, cutter (c)
$(\mu_c)^{(c)}$, **rc_fric(** n_c **)**	FLT	$[0.0,\infty)$	0.0	cutter-rock friction coefficient, cutter (c)

Table 2 Cutting-Test Parameters (2 of 2)

Parameter	Type	Range	Default	Description
Cutting-test properties are listed via **@rcListProps**.				
Chaining-algorithm group				
B_c, **ch_on**	BOOL	$\{\text{true}, \text{false}\}$	false	chaining active
B_s, **ch_seal**	BOOL	$\{\text{true}, \text{false}\}$	false	chain seals active
$f_b^{(c)}$, **ch_facBack(** n_c **)**	INT	$\{0,1,\ldots,n_f^{(c)}\}$	0	back-face facet, cutter (c) (seal does not form on this facet; if zero, then no facet is excluded)
P, **ch_Ps**	FLT	$[0.0,\infty)$	0.0	confining pressure
g, **ch_gap**	FLT	$[0.0,\infty)$	0.0	chain gap (chain balls are within this distance of one another)
N_c, **ch_Nc**	INT	$[1,\infty)$	500	chain-regeneration interval
t_p, **ch_pause**	FLT	$[0.0,\infty)$	0.0	pause time (seconds) during chain generation
$\varepsilon_{\lim}$, **ch_ARatLimit**	FLT	$(0.0,\infty)$	1×10^{-5}	equilibrium-ratio limit

				(parameter of **ft_eq**)
$n_{\lim}$, **ch_stepLimit**	INT	$[1,\infty)$	1×10^{-6}	step limit (parameter of **ft_eq**)
Control and monitoring group				
t_l, **rcLayerThick**	FLT	$(0,\infty)$	H	horizontal-layer thickness (material-vessel height: H)
M_d, **rcDeterministic**	BOOL	$\{\text{true},\text{false}\}$	false	deterministic mode
R_h, **rcHistUpdateRate**	INT	$[1,\infty)$	100	history sampling interval
R_E, **rcEnergyUpdateRate**	INT	$[1,\infty)$	100	energy-quantity sampling interval
o_v, **rcVacTopOS**	FLT	$(0,\infty)$	H	vacuum box top offset (from rock surface)
R_v, **rcVacUpdateRate**	INT	$[1,\infty)$	5000	vacuum update interval
R_{ps}, **msUpdateRate**	INT	$[1,\infty)$	1×10^{6}	microstructural PS update interval
$\mathbf{x}_b$, **rc_msBoxCtr**	VEC2	$[\mathbb{R},\mathbb{R}]$	$(0,0)$	microstructural box center
$\mathbf{d}_b$, **rc_msBoxDims**	VEC2	$[\mathbb{R},\mathbb{R}]$	$(1,1)$	microstructural box dimensions
g_f, **ckFilterGap**	FLT	$(-\infty,\infty)$	0.0	crack-filtering gap
R_c, **ckUpdateRate**	INT	$[1,\infty)$	1×10^{6}	crack geometry update interval

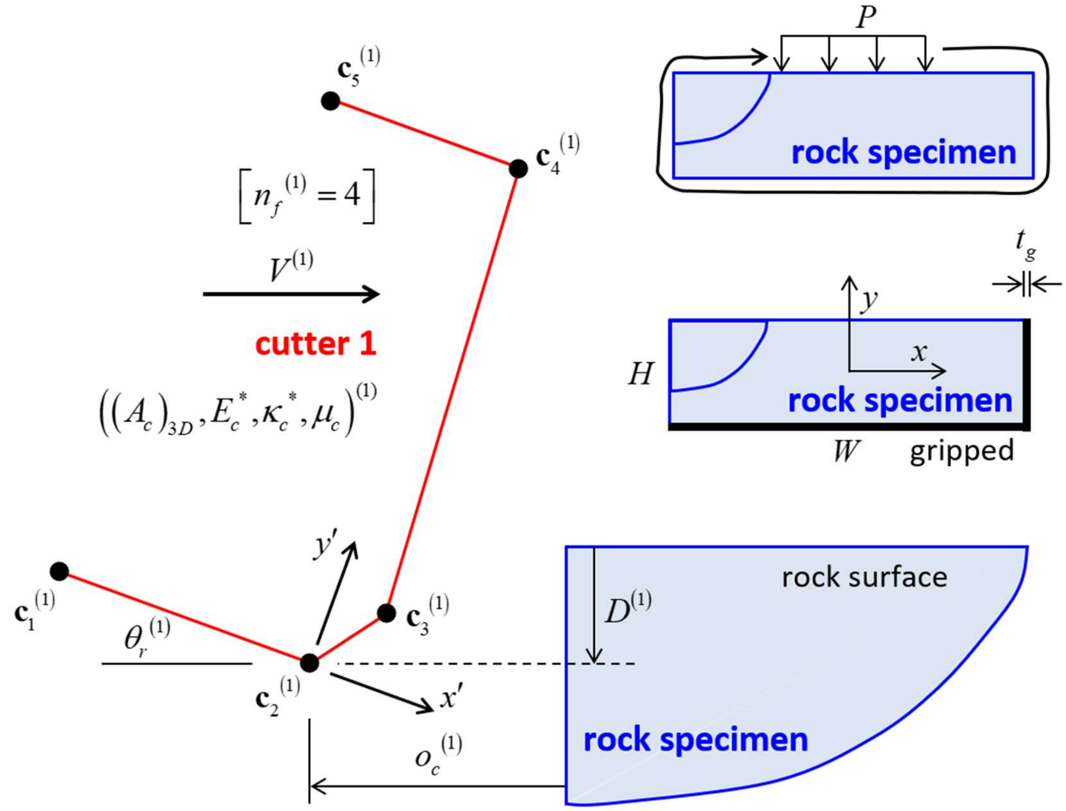

Figure 2 ***Cutting-test model showing first cutter and rock specimen. The second cutter is located behind the first cutter.***

Each cutter consists of a single wall composed of linear facets, and the initial positions of the facet vertices are expressed in terms of the cutting-test parameters (Newman and Sproull, 1979, p. 58):

$$\begin{bmatrix} c_{ix} & c_{iy} & 1 \end{bmatrix} = \begin{bmatrix} c'_{ix} & c'_{iy} & 1 \end{bmatrix} \begin{bmatrix} \cos\theta_r & -\sin\theta_r & 0 \\ \sin\theta_r & \cos\theta_r & 0 \\ 0 & 0 & 1 \end{bmatrix} \begin{bmatrix} 1 & 0 & 0 \\ 0 & 1 & 0 \\ T_x & T_y & 1 \end{bmatrix}, \quad i = \{1, 2, \ldots, n_f + 1\} \tag{1}$$

$$\text{with} \quad T_x = \frac{-W}{2} - o_c, \; T_y = \frac{H}{2} - D.$$

The cutting test consists of a set-up phase followed by a cutting phase. During the set-up phase, the grip grains are identified and fixed, the confining pressure is applied, the cutter walls are created and their interaction with the rock is specified, and the model domain is expanded to accommodate the cutter-rock system. The model state is saved at the end of the set-up phase.

During the cutting phase, the cutter walls are moved parallel with the rock surface at the specified velocities $\left(V^{(c)}\right)$. The cutting phase consists of multiple stages during which the displacement increments of the first cutter ($\Delta\delta_x^{(1)}, \Delta\delta_x^{(1)} > 0$ is moving to the right) are specified in the function

rcPerformStages. The model state is saved, and crack geometry is updated at the end of each stage.

1.2 System-Behavior Quantities

During the cutting test, the crack-monitoring package is on, and the system behavior is monitored using the history mechanism to sample and store relevant quantities (see Table 3). The monitored quantities include cutter displacement $\left(\boldsymbol{\delta}^{(c)}\right)$, cutter force $\left(\mathbf{F}^{(c)}\right)$, displacement-averaged cutter force $\left(\tilde{\mathbf{F}}^{(c)}\right)$, cutting time (t), and the energy quantities.

Table 3 System-Behavior Quantities

Quantity, *FISH*	Description
$\boldsymbol{\delta}^{(c)}$, **rc_disp{X,Y}{1,2}**	cutter displacement, cutter (c)
$\mathbf{F}^{(c)}$, **rc_force{X,Y}{1,2}**	cutter force, cutter (c)
$\tilde{\mathbf{F}}^{(c)}$, **rc_forceAvg{X,Y}{1,2}**	displacement-averaged cutter force, cutter (c)
t, **rc_time**	cutting time
Energy quantities	
Obtain energy partitions via **rcCheckEnergies**.	
Input energy group	
E_c, **rc_Ecut**	cutter energy (total, $\mathrm{E}_c = \mathrm{E}_c^{(1)} + \mathrm{E}_c^{(2)}$)
$\mathrm{E}_c^{(c)}$, **rc_Ecut{1,2}**	cutter energy, cutter (c)
E_p, **rc_Ep**	pressure energy
$(e_c)_{2D}^{(c)}$, **rc_Emse2D{1,2}**	2D mechanical specific energy, cutter (c)
$(e_c)_{3D}^{(c)}$, **rc_Emse3D{1,2}**	3D mechanical specific energy, cutter (c)
Stored energy group	
E_k, **rc_Estr**	strain energy (total, $\mathrm{E}_k = \mathrm{E}_k^r + \mathrm{E}_k^{cr}$)
E_k^r, **rc_EstrR**	strain energy in rock
E_k^{cr}, **rc_EstrCR**	strain energy in cutter-rock interfaces
$\mathrm{E}_k^{cr(c)}$, **rc_EstrCR{1,2}**	strain energy in cutter-rock interface, cutter (c) (to measure set **rc_EstrCRboth = 1**)
E_m, **rc_Emot**	kinetic energy in rock
Dissipated energy group	
E_μ, **rc_Eslip**	slip energy (total, $\mathrm{E}_\mu = \mathrm{E}_\mu^r + \mathrm{E}_\mu^{cr}$)

E_{μ}^{r}, **rc_EslipR**	slip energy in rock
E_{μ}^{cr}, **rc_EslipCR**	slip energy in cutter-rock interfaces
$\mathrm{E}_{\mu}^{cr(c)}$, **rc_EslipCR{1,2}**	slip energy in cutter-rock interface, cutter (c) (to measure set **rc_EslipCRboth = 1**)
E_{b}, **rc_Ebond**	bond-breakage energy
E_{v}, **rc_Evac**	vacuumed energy
E_{α}, **rc_Edamp**	local-damping energy

Cutter displacement is the position of the cutter relative to its initial position:

$$\boldsymbol{\delta} = \mathbf{c} - \mathbf{c}_{\mathbf{o}} \tag{2}$$

where $\mathbf{c}$ is the cutter position defined by the cutter-facet vertex that is farthest below the rock surface,[7] and $\mathbf{c}_{\mathbf{o}}$ is the initial cutter position. Cutting time is the elapsed time since the start of the test.

Cutter force,

$$\mathbf{F} = \left(F_x, F_y\right) \tag{3}$$

is the total force exerted by the rock on the cutter and is obtained by summing the contact forces at the cutter-rock interface, where F_x and F_y are the x and y components, respectively, of the total force on the cutter wall. The total force exerted by the cutter on the rock is $-\mathbf{F}$. The displacement-averaged cutter force ("Cumulated moving average," 2026)

$$\tilde{\mathbf{F}}(x) = \frac{\int_{x_o}^{x} \mathbf{F}\,dx}{\int_{x_o}^{x} dx} \tag{4}$$

is the average cutter force of all the data up until the current datum. The response reaches a steady state when $\tilde{\mathbf{F}}$ remains constant.

[7] If a cutter-facet vertex lies at the reference point used to orient and position the cutter, then the cutter-facet vertex used to define cutter position will coincide with the reference point.

The energy quantities monitored during the test are listed in Table 3. The energy input to the cutter-rock system is the cutter energy ($\mathrm{E}_c, \mathrm{E}_c \geq 0$) and the pressure energy ($\mathrm{E}_p, \mathrm{E}_p \geq 0$). The cutter energy is the work done by the cutter on the rock:

$$\mathrm{E}_c = -\int \mathbf{F} \cdot d\boldsymbol{\delta} \tag{5}$$

The cutter energy is zero at the start of the test and increases as the test proceeds. The cutter energy expended as the cutter moves parallel to the rock surface by a distance of s is given by

$$\mathrm{E}_c(s) = -\int_s \mathbf{F} \cdot d\boldsymbol{\delta} = -\int_{x_o}^{x} F_x \, dx, \quad s = x - x_o \tag{6}$$

The pressure energy is the work done by the confining pressure on the rock:

$$\mathrm{E}_p = \sum_p \left(\int \mathbf{F}^{(p)} \cdot d\boldsymbol{\delta}^{(p)} \right) \tag{7}$$

where $\mathbf{F}^{(p)}$ is the external force applied to chain particle (p), and $\boldsymbol{\delta}^{(p)}$ is the displacement of chain particle (p). The pressure energy is accumulated during the test. A positive pressure energy exists at the start of the test because of the initial pressure application that compresses the initially stress-free block of material. A negative pressure energy indicates that energy is exiting the cutter-rock system and compressing the fluid.

The mechanical specific energy (MSE, e_c, $e_c \geq 0$) is the energy required to remove a unit volume of rock:

$$e_c = \frac{\mathrm{E}_c}{V_c} = \frac{\mathrm{E}_c}{A_c\, s}, \quad A_c = \begin{cases} D\,t, & (\text{2D model: } t \equiv 1) \\ (A_c)_{\text{3D}}, & \text{3D area of cut} \end{cases} \tag{8}$$

where V_c is the volume of removed rock; A_c is the area of cut; D is the depth of cut; t is the thickness of the rock specimen (always equal to one in the 2D model); $(A_c)_{\text{3D}}$ is the area of the removed-rock volume that is perpendicular to the rock surface (defined by the red area in Fig. 10 of Blanksma and Potyondy (2015) — the value of d in Eq. (4) of Blanksma and Potyondy (2015) is not defined; thus, $(A_c)_{\text{3D}}$ is an input parameter); and s is the cutter displacement parallel to the rock surface. The MSE can also be expressed as the displacement-averaged horizontal cutter force $\left(\tilde{F}_x\right)$ divided by the area of cut:

$$e_c = \frac{\mathrm{E}_c}{V_c} = \frac{-\int_{x_o}^{x} F_x \, dx}{A_c \int_{x_o}^{x} dx} = -\frac{\tilde{F}_x}{A_c} \tag{9}$$

Two values of MSE are computed: $(e_c)_{\mathrm{2D}}$ corresponds with the use of a 2D-based area of cut, and $(e_c)_{\mathrm{3D}}$ corresponds with the use of a 3D-based area of cut (which corresponds with the physical cylindrical cutter).[8]

The stored energies are strain energy $(\mathrm{E}_k,\ \mathrm{E}_k \ge 0)$ and kinetic energy $(\mathrm{E}_m,\ \mathrm{E}_m \ge 0)$. The strain energy is partitioned into the strain energy in the rock and cutter-rock interface. The strain energy is stored in the springs at the ball-ball and facet-ball contacts. Expressions for the strain energy are given in Itasca (2026a).[9] The kinetic energy is associated with the motion of the grains:

$$\mathrm{E}_m = \frac{1}{2}\sum_{\text{grains}} \left(mv^2 + \left[\tfrac{1}{2} mR^2 \right] \omega^2 \right) \tag{10}$$

where m, v, R, and ω are the mass, translational velocity, radius, and rotational velocity of each grain (which is a disk). The strain and kinetic energies are zero at the start of the test and fluctuate about positive values as the test proceeds.

The dissipated energies are slip energy $(\mathrm{E}_\mu,\ \mathrm{E}_\mu \ge 0)$, bond-breakage energy $(\mathrm{E}_b,\ \mathrm{E}_b \ge 0)$, vacuumed energy $(\mathrm{E}_v,\ \mathrm{E}_v \ge 0)$, and local-damping energy $(\mathrm{E}_\alpha,\ \mathrm{E}_\alpha \ge 0)$. The slip energy is partitioned into the slip energy in the rock and cutter-rock interface. The slip energy is the total energy dissipated by frictional slip at the ball-ball and facet-ball contacts (see Figure 3). Expressions for the slip energy are given in Itasca (2026).[10] The slip energy is zero at the start of the test and increases as the test proceeds.

[8] Preliminary results indicate that $(e_c)_{\mathrm{3D}}$ matches the 3D physical behavior much better than $(e_c)_{\mathrm{2D}}$. The use of $(e_c)_{\mathrm{3D}}$ may be justified as a means of obtaining this 3D information from the 2D model; however, further justification should be obtained.

[9] In documentation set at PFC - PFC Model Objects - Contacts and Contact Models - Contact Models - Built-in Contact Models - {Linear Model, Linear Parallel Bond Model} - Energy Partitions.

[10] In documentation set at PFC - PFC Model Objects - Contacts and Contact Models - Contact Models - Built-in Contact Models - {Linear Model, Linear Parallel Bond Model} - Energy Partitions.

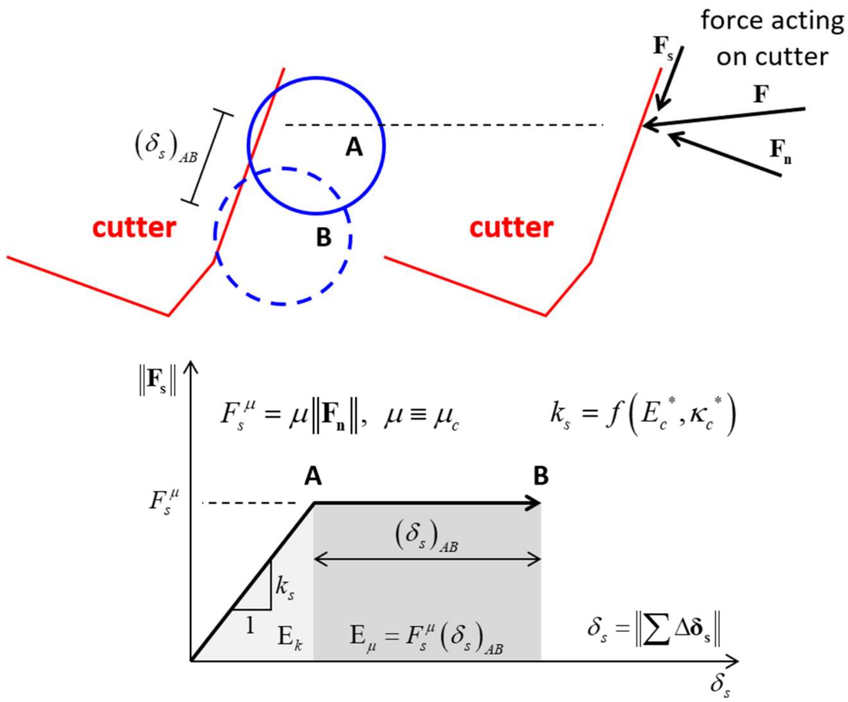

Figure 3 ***Definition of slip and strain energies (as shaded regions under the force-displacement curve) for a grain sliding along the cutter with a constant overlap.***

The bond-breakage energy is the sum of the strain energy in each parallel bond at the time of its breakage:

$$\mathrm{E}_b = \sum_{\substack{\text{broken} \\ \text{pbonds}}} \overline{\mathrm{E}}_k \tag{11}$$

where $\overline{\mathrm{E}}_k$ is the bond strain energy given by Eq. (15) in Itasca (2026a).[11] The bond-breakage energy is removed from the model when the bond breaks. The bond-breakage energy is zero at the start of the test and increases as the test proceeds.

The vacuumed energy is the sum of the kinetic energy of each grain at the time of its deletion. The vacuumed energy is removed from the model when the grain is deleted. The vacuumed energy is zero at the start of the test and increases as the test proceeds.

The local-damping energy is the sum of the work done on each grain by the local-damping force:

$$\mathrm{E}_\alpha = \sum_{\text{grains}} \mathbf{F}_\alpha \cdot \boldsymbol{\Delta} \tag{12}$$

[11] In documentation set at PFC - PFC Model Objects - Contacts and Contact Models - Contact Models - Built-in Contact Models - Linear Parallel Bond Model - Energy Partitions.

where $\mathbf{F}_\alpha$ is the generalized damping force (given by Eq. (2) in Itasca [2026a][12]) that is always directed to oppose motion, and $\mathbf{\Delta}$ is the generalized displacement of the grain — the generalized quantities contain a term for each degree of freedom, and this force and displacement occur over each timestep. The local-damping energy is computed as[13]

$$E_\alpha = E_c + E_p - \left(E_k + E_m + E_\mu + E_b + E_v\right). \quad (13)$$

The local-damping energy is zero at the start of the test and increases as the test proceeds.

1.3 Wet Cutting

In a real borehole, drilling mud produces a pressure that acts on the rock surface and effectively strengthens the rock, thereby greatly increasing the energy requirements of drilling. The postulated mechanism that explains this behavior is outlined in the remainder of this paragraph, because it guides the development of the pressure-application scheme. The cutter is held at a fixed depth of cut and moved across the rock surface. After an initial period of damage formation, the cutter-rock system reaches a steady-state condition in which the cutter is no longer in contact with virgin rock, but instead, is bearing against broken material. The damaged region extends in front of and slightly below the cutter, and the broken material is forced to flow around and beneath the cutter. For confined conditions corresponding with wet cutting, the broken material consists of very small fragments that are compressed tightly together as they extrude up the cutter face and flow around and beneath the cutter; whereas, for unconfined conditions corresponding with dry cutting, the broken material consists of relatively large fragments that are nearly uncompressed as they flow around and beneath the cutter. We suggest that it is the difference in both the damage and material-flow processes that increase the energy requirements of drilling for wet cutting — i.e., it takes more energy to create the very small fragments and force them to flow past the cutter.

A 2D pressure-application scheme, denoted as the chaining algorithm, simulates the effect of drilling mud by continually identifying a connected chain of particles on the rock surface and applying a pressure to those particles as the cutting process proceeds. This pressure inhibits chip formation and leads to a more plastic-like zone of damage that remains near the cutter. We desire a robust and automatic procedure for applying a pressure boundary condition to the rock surface during the cutting process. An ideal procedure would mimic the real process by which drilling mud loads a rock surface during cutting. We envision the process to occur as follows.

Drilling mud is a viscous liquid, and the load it provides to the rock surface can be characterized by a pressure. How does this pressure load the rock? The mud coalesces into a membrane structure that lies on top of the rock surface and bridges across pores in the rock and crushed

[12] In documentation set at PFC - Numerical Simulations with PFC - PFC Model Formulation - Energy and Dissipation Mechanisms in PFC.
[13] The local-damping energy is computed by summing all energies in the system and noting that the only energy term not measured directly is the local-damping energy.

rock particles that form in front of a cutter. The membrane structure defines a surface that transmits normal load to the rock material.[14] This surface evolves during the cutting process. Envision a membrane initially lying on the rock surface with pressurized fluid on the non-rock side. The membrane transmits the fluid pressure to the rock and stays in contact with the rock material (conforming to and thereby defining the surface) as it is broken and deformed by the cutter. The membrane can be thought of as a magic blanket that remains in intimate contact with the evolving rock surface, serving to both define and confine the rock surface. The rock surface is loaded by both the membrane and the cutter. The cutter interacts with the rock, but not with the membrane.

The chaining algorithm mimics the process envisioned above by identifying a connected chain of particles that is in contact with, and loaded by, a membrane structure that lies along the particle centers. The spanning chain defines both the rock surface and the membrane structure. The spanning chain can be constructed unambiguously for two-dimensional particle assemblies lying in a plane, because given a particle in the chain, all contacts of that particle can be ordered circumferentially, and the next contact in a specified direction defines the next particle in the chain. As all information is topological, there is no need to perform geometric queries; thus, the topological data structure provided by PFC2D (which provides ball and wall adjacencies via ball-ball and ball-wall contacts) allows one to implement this algorithm in a robust fashion — i.e., the algorithm will never fail, no matter how complex the surface shape becomes.

For three-dimensional particle assemblies lying in three-dimensional space, the concept of a spanning chain becomes a spanning surface. Such a surface cannot be constructed by relying on topological information alone, because the ordering of contacts about a surface particle is ambiguous. The adjacent particles on the surface cannot be found by relying solely on contact ordering, but instead, require information about the outside of the body to ensure that each adjacent particle lies on the body surface. However, the body surface is not known in advance; it will be defined by the spanning surface. It may be possible to develop a relatively robust 3D spanning-surface algorithm, but this has not been done. Instead, an alternative procedure that is guaranteed to be robust and does not rely upon topological adjacency information has been developed. The three-dimensional pressure-application procedure is referred to as the shining-lamp algorithm, because it defines the surface particles as those that receive direct illumination[15] from light sources that surround and shine toward the body (Potyondy, 2012). Each surface particle is assigned an externally applied force that is related to the specified pressure and the amount of light that it receives (which is related to its illuminated surface as shown in Figure 4). A 3D wet-cutting model that uses the shining-lamp algorithm is shown in the upper-left image of Figure 1. The shining-lamp algorithm has been used by Schöpfer et al. (2017) to apply constant overburden pressure to the surface of a model used to study normal fault growth in layered sequences of strong layers (bonded particles) and weak layers (nonbonded particles) as shown in Figure 4.

[14] The membrane-rock interface is assumed to be frictionless; thus, only normal load is transferred across the interface.
[15] Indirect illumination produced by reflection of light rays is not considered.

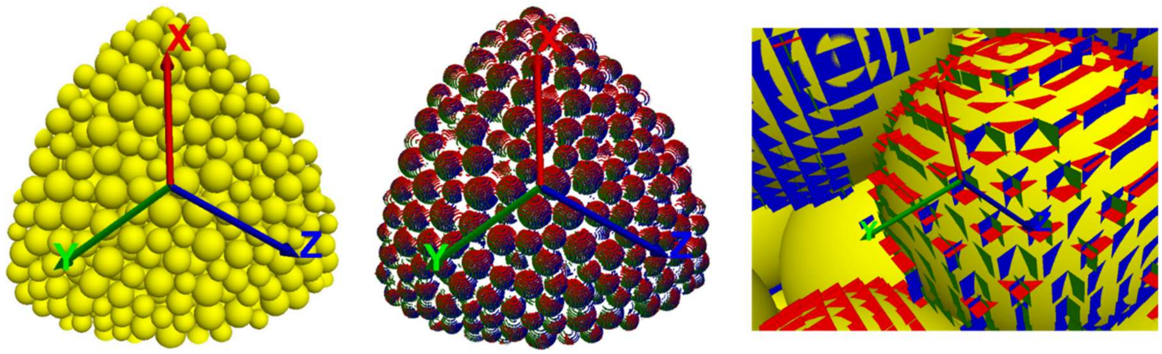

Figure 4 ***Grains in the positive octant of a bonded spherical body (left) and grain surfaces illuminated by red, green, and blue light sources directed along the x, y, and z axes, respectively (center and right).*** (From Figs. 9, 11, and 14 of Potyondy [2012])

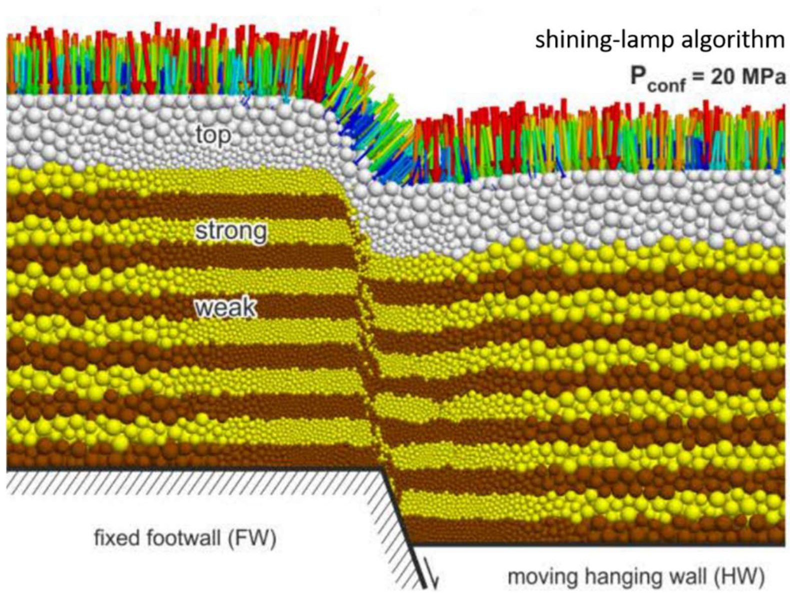

Figure 5 ***PFC3D model (side view) of normal fault development showing faulted model at a throw of three strong layer thicknesses with material regions colored yellow (strong), brown (weak), and white (top layer).*** (From Fig. 7 of Schöpfer et al. [2017])

The two-dimensional pressure-application procedure developed for this project is referred to as the chaining algorithm. The chaining algorithm creates a chain that encloses a cluster of balls. The initial cluster is the bonded specimen, and the cluster evolves as the cutting test proceeds (see Figure 6). The chain begins at a specified surface ball (taken as the grip grain at the bottom-right corner of the specimen) and proceeds in a counter-clockwise direction around the cluster until it returns to this ball. The chain consists of an ordered list of balls joined by existing contacts[16] within a specified gap of one another. The chain gap affects the chain topology by controlling how the chain bridges across rock pores and rock fragments. The chain is oriented such that the outside is to the right of the chain that traverses the cluster surface in a counter-clockwise direction. The chain defines a surface that spans between the centers of contiguous balls. The surface is loaded by a specified pressure that acts from the outside. The pressure is mapped to an applied external force acting on each chain ball, with the force magnitude and direction determined by the local surface geometry and pressure. The chain is visualized by marking the chain balls, joining their centers with straight lines, and drawing the applied external forces as arrows. Details of the chaining algorithm are provided in Figures 7–11. If chain seals are activated, then a seal is formed at each cutter-rock interface such that pressure cannot penetrate. The seal extends from the first to last balls in compressive contact with each cutter, and the back-face facet may be excluded from consideration. Pressure is not applied to the chain segments between sealed balls.

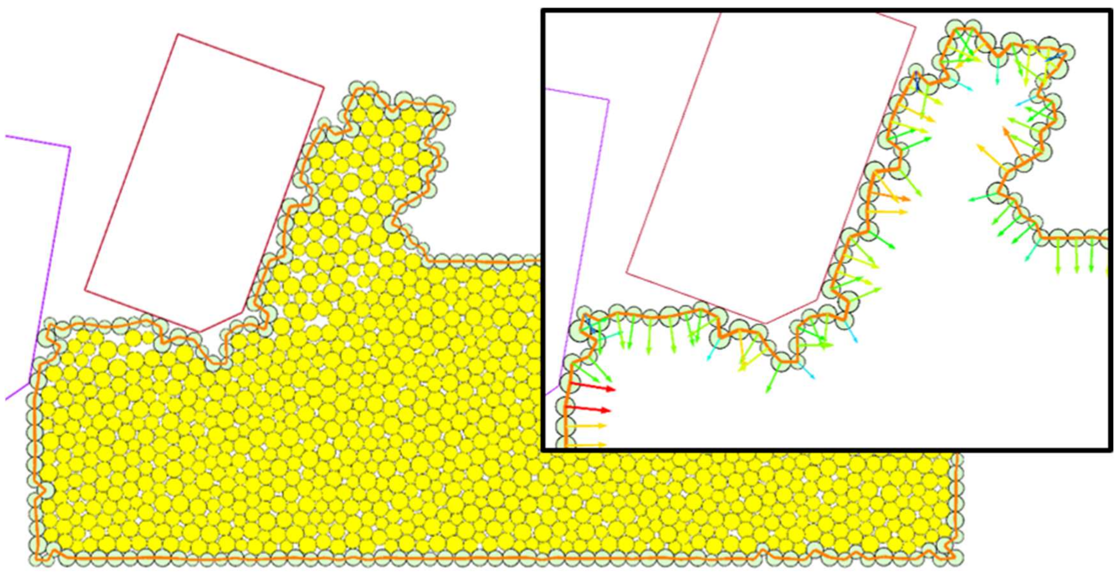

Figure 6 Pressure-application chain (no chain seals) with 5-MPa confining pressure acting on the base case cutting-test model showing chain balls, chain links, and applied external forces.

[16] The contacts are existing at the time of chain formation and force application. During subsequent cycling some of these contacts may be deleted in which case the chain links will not be drawn; however, the applied external forces continue to act on the chain balls. The chain-regeneration interval is specified via **`ch_Ns`**.

Precondition
A contact exists between all balls with a contact gap (gc, minimal signed distance between the contacting balls) less than or equal to the chain gap (g). The contacts around a ball are ordered in a counter-clockwise direction. There are two balls associated with each contact.

Initial Condition
Specify the starting ball (b1). Find the next contact (c1) and ball (b2) of the chain as follows. c1 is the first contact of b1 in the counter-clockwise direction from the positive x-axis that has a contact gap less than or equal to the chain gap. b2 is the other ball (not b1) associated with c1.

Continuation Condition
Given a ball at the head of the chain (b2) and its previous contact (c1). Find the next contact (c2) and ball (b3) of the chain as follows. c2 is the first contact of b2 in the counter-clockwise direction from c1 that has a contact gap less than or equal to the chain gap (c2 may equal c1 in which case the chain wraps back on itself — see particle string in subsequent figure). b3 is the other ball (not b2) associated with c2. Update the ball at the head of the chain and its previous contact until the ball at the head of the chain equals b1.

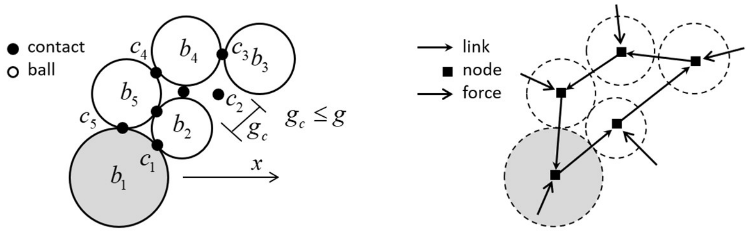

The chain encloses a cluster of balls and consist of links that join nodes. Pressure acts upon the cluster as follows. Pressure acts on each link to produce a force (pressure times link length times unit thickness) directed perpendicular to the link. The force is distributed equally to the nodes at its ends. The total force at each node is applied as an external force to the ball associated with the node.

Figure 7 Chaining-algorithm description.

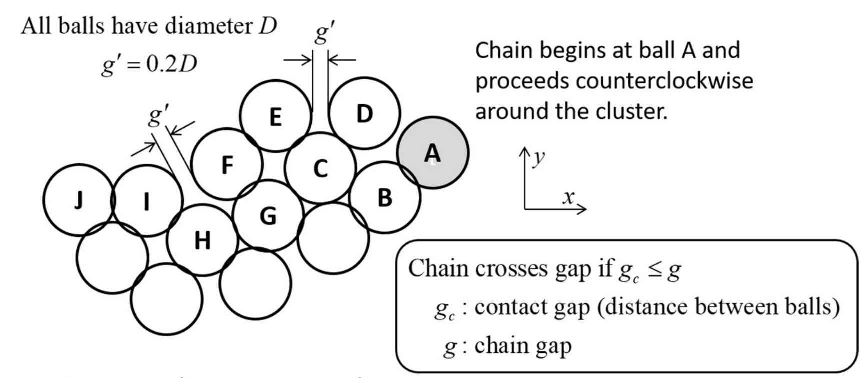

$g = g' \Rightarrow$ chain $\{A, D, E, F, I, J \ldots\}$

$g = 0 \Rightarrow$ chain $\{A, B, C, D, C, E, F, G, H, I, J \ldots\}$

Figure 8 Chaining algorithm showing how the chain gap affects chain topology.

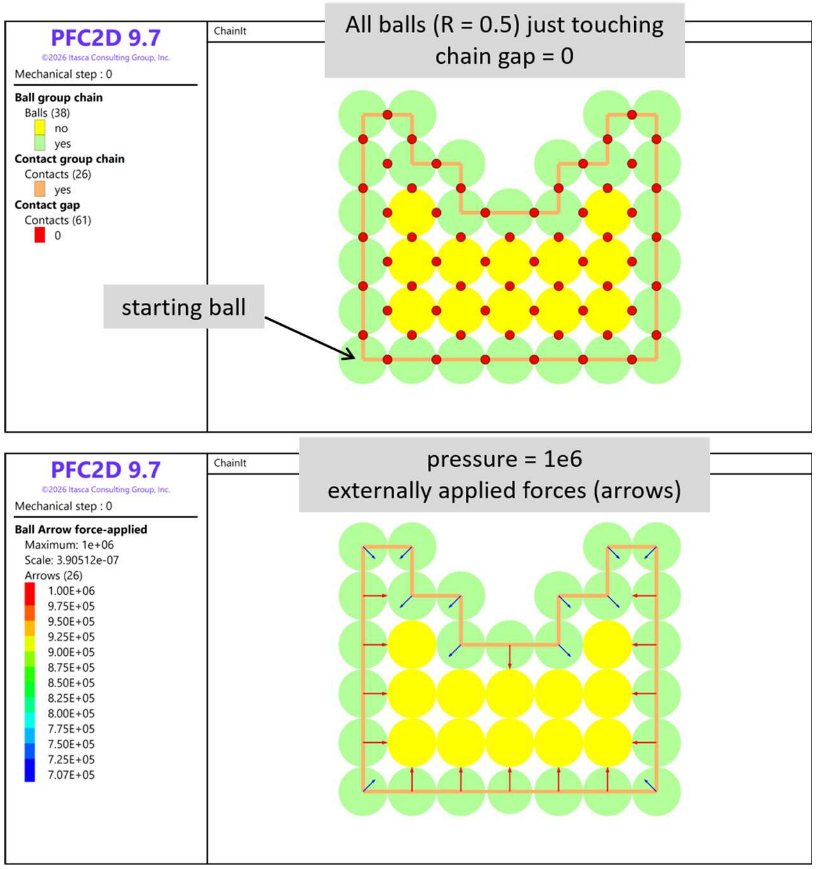

Figure 9 ***Chaining algorithm showing chain (top) and applied external forces (bottom) for simple model.***

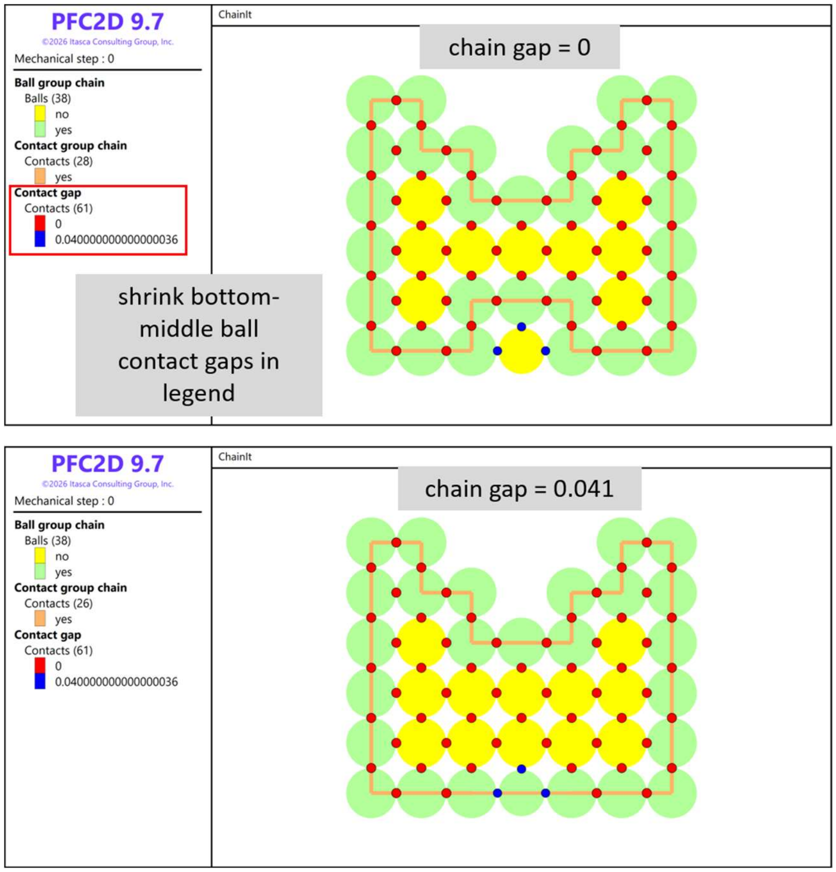

Figure 10 ***Chaining algorithm showing effect of chain gap on modified simple model. The chain bridges the gap when the contact gap is less than or equal to the chain gap.***

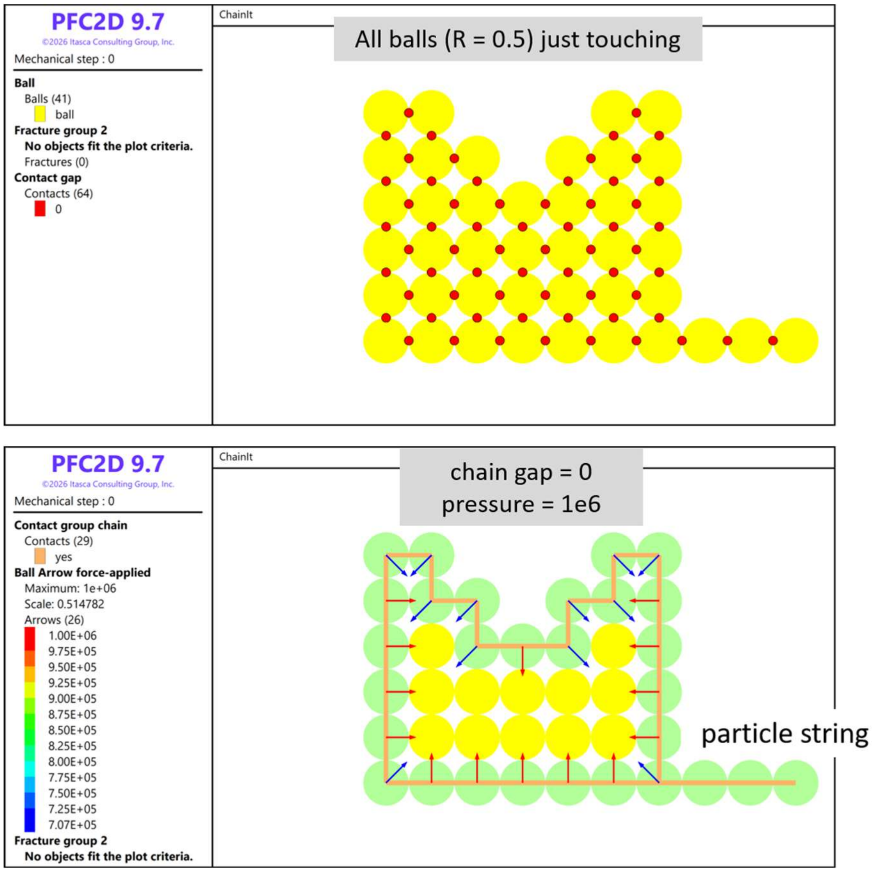

Figure 11 Chaining algorithm showing how the applied external forces cancel one another for a string of particles resulting in no load on the string.

The behavior of the chaining algorithm is illustrated in Figures 12 and 13. The chain gap controls how the chain bridges between balls (see Figure 12). If the chain gap is zero, then the broken material does not remain confined, but instead escapes from the confined surface. Setting the chain gap equal to 20 percent of the average grain diameter effectively confines the broken material. The chain evolution is illustrated in Figure 13.

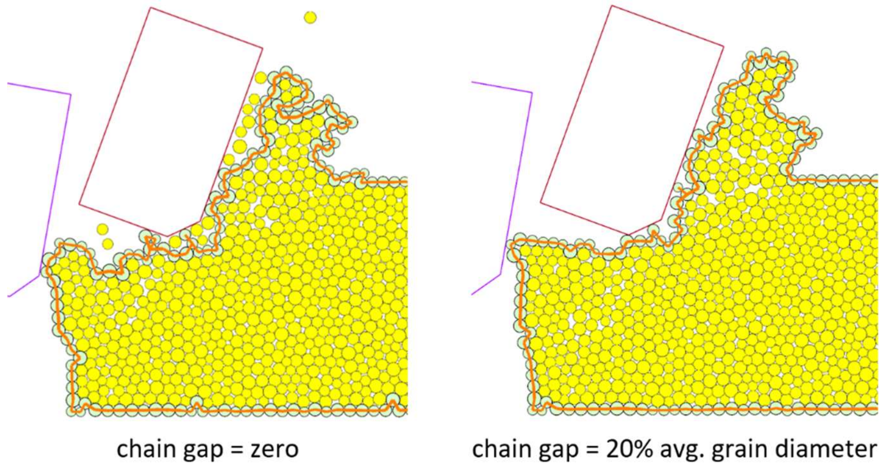

Figure 12 ***Effect of chain gap on chaining-algorithm behavior (no chain seals) for the base case cutting-test model subjected to 5-MPa confining pressure.***

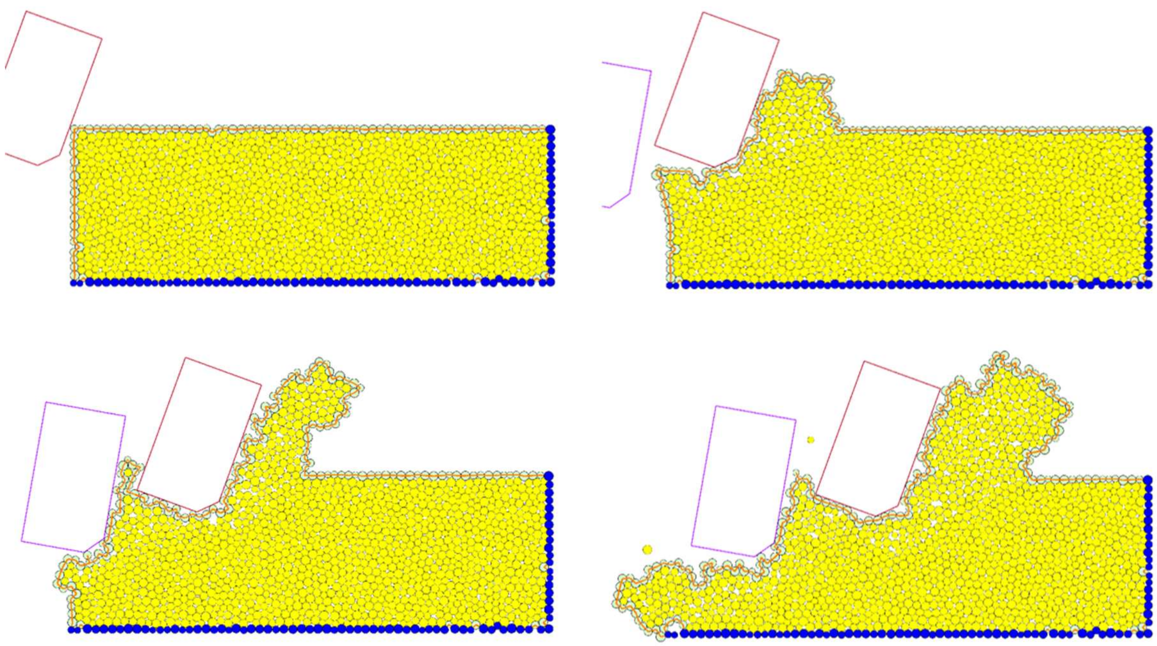

Figure 13 ***Evolution of pressure-application chain (no chain seals) for cutter-1 displacements of 0, 2, 4, and 6 mm for the base case cutting-test model subjected to 5-MPa confining pressure, and with a chain gap equal to 20 percent of the average grain diameter. The x***

The behavior of the chain-seal logic is illustrated in Figures 14 and 15. When chain seals are active, and the back-face facet is excluded from consideration, then the grains remain in intimate contact with the cutter. Pressure is not applied to the chain segments between sealed balls, and these balls tend to line up along the cutter face.

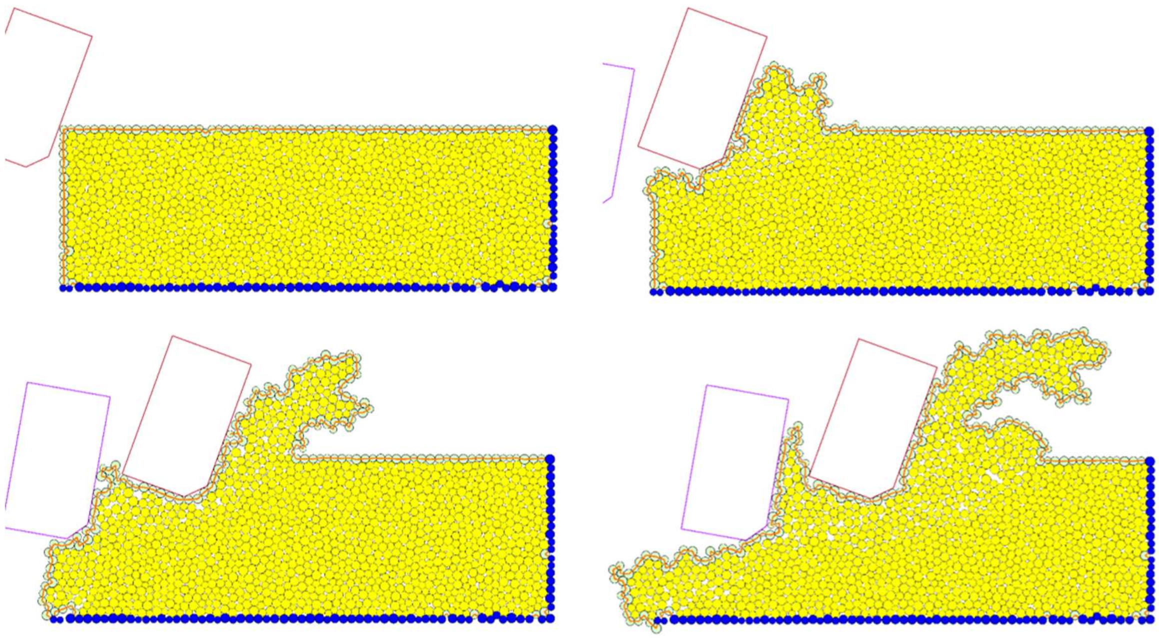

Figure 14 ***Evolution of pressure-application chain (with chain seals) for cutter-1 displacements of 0, 2, 4, and 6 mm for the base case cutting-test model subjected to 5-MPa confining pressure, and with a chain gap equal to 20 percent of the average grain diameter.***

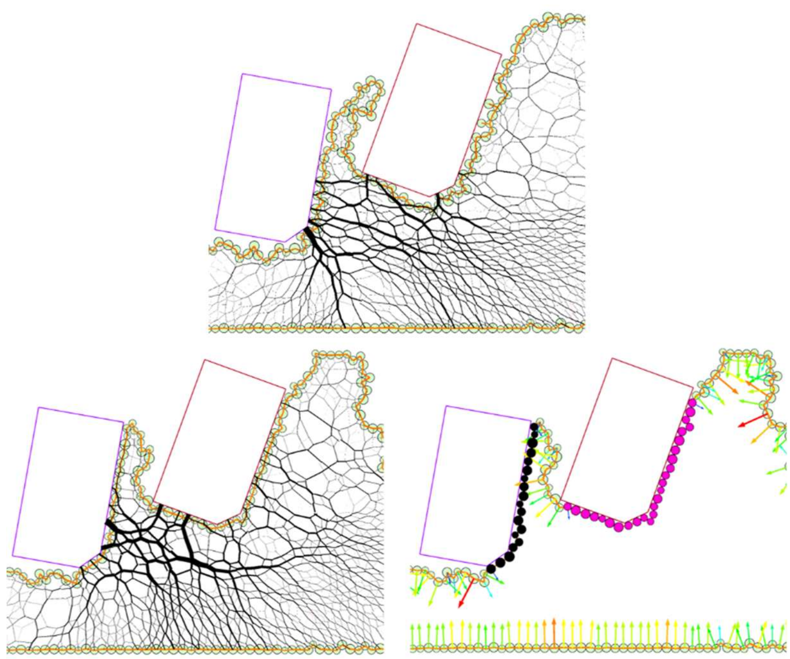

Figure 15 ***Force-chain fabric, seal balls, and applied external forces with 5-MPa confining pressure acting on the base case cutting-test model.***

2.0 SYNTHETIC MATERIAL

The synthetic material is a 2D parallel-bonded material that represents Torry Buff sandstone. Potyondy and Blanksma (2015, Section 3: MODEL DESCRIPTION) provide a thorough description of this model. The description of a parallel-bonded material is being updated to coincide with that of the flat-jointed material in Potyondy (2026). The updated description is given in the first two subsections and used in the third subsection to list the microproperties of the Torry Buff material. The material response during direct-tension, biaxial compression, and rock cutting is described in the third subsection.

2.1 Material Genesis

The material-genesis procedure is shown in Figure 16. The parallel-bonded material is created within a material vessel by packing together a cloud of particles from a given size distribution to material pressure $(P_m > 0)$ using the linear contact model. The number of contacts at the end of the packing phase is controlled by P_m such that increasing P_m increases the number of contacts. Additional contacts are created to fill the gaps between particles by specifying a positive interaction gap $(g_i > 0)$ as shown in Figure 17.[17] The granular material is then transformed into a parallel-bonded material by assigning the parallel-bonded material properties to all contacts, but only those contacts with a gap less than or equal to the interaction gap are bonded. The particle connectivity is controlled by the material pressure and the interaction gap, with the interaction gap being of primary importance.

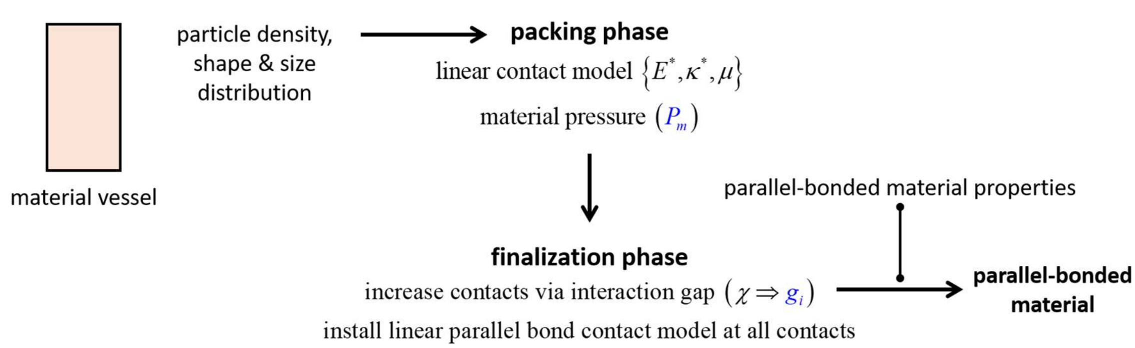

Figure 16 Material-genesis procedure to produce a parallel-bonded material.

[17] Contacts will exist between all particles with a gap less than or equal to the interaction gap.

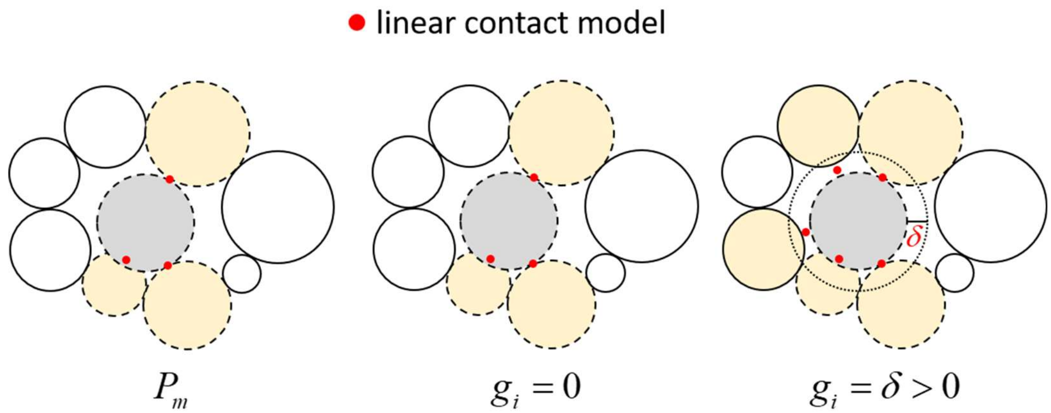

Figure 17 Particle assembly after packing at material pressure (left), applying an interaction gap of zero (middle), or applying a positive interaction gap (right).

The interaction gap (g_i) may be specified relative to the median particle size

$$g_i = \chi d_{50} \tag{14}$$

where χ is the interaction-gap coefficient and d_{50} is the median particle size (see Figure 18). If the interaction-gap coefficient becomes too large, then one may obtain an overly connected microstructure for which the faces between connected grains overlap one another (see Figure 19 and discussion associated with this figure in the cited document).

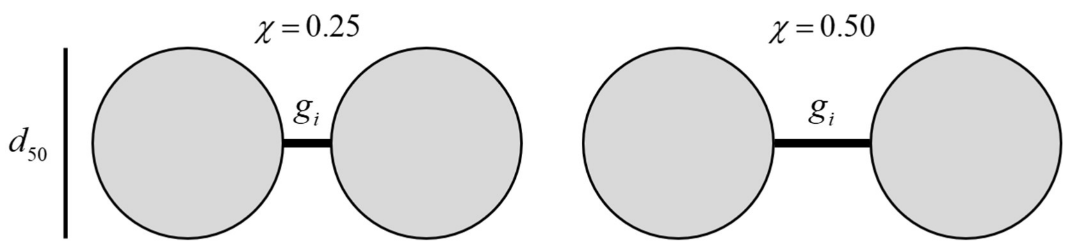

Figure 18 Interaction gap relative to median particle size for interaction-gap coefficients of 0.25 (left) and 0.50 (right).

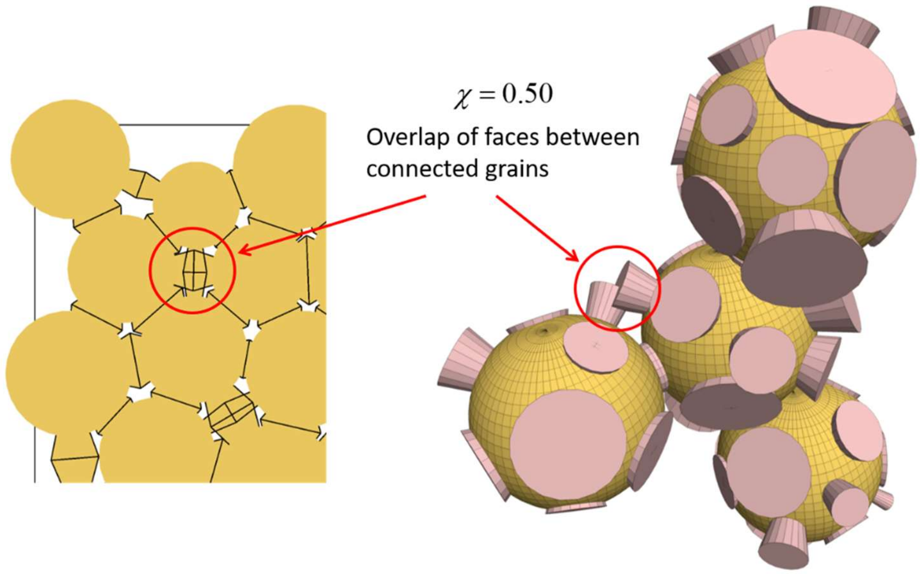

Figure 19 Flat-jointed materials with overly connected microstructures obtained with interaction-gap coefficient of 0.5. (From Fig. 31 of Potyondy [2026])

2.2 Parallel-Bonded Material Parameters

A parallel-bonded material is defined by the primary parameters in Figure 20 and Table 4. The primary parameters (consisting of parameter names and symbols) are those that should be listed when describing a particular instance of a parallel-bonded material — e.g., in a report or journal paper. The **particle parameters** specify the density and size distribution of the particles. The **packing parameters** specify packing pressure, local-damping factor of all particles, and deformability and strength of the linear contact model that defines the granular material during the packing phase and will be assigned to new contacts that form after the bonds have been installed in the finalization phase. The **ensemble parameter** specifies a property that applies to the ensemble of packed particles: interaction-gap coefficient to create contacts in the gaps between the packed particles. The **parallel-bond model parameters** specify the deformability and strength properties that are assigned to the particle-particle interfaces.

ensemble	parallel-bond model				
size of cement	surface-surface		cement		
$\left\{ \overline{\lambda} \Rightarrow \overline{R};\right.$	$\left[E^*, \kappa^*\right] \Rightarrow \left[k_n, k_s\right];$	$\mu;$	$\left[\overline{E}^*, \overline{\kappa}^*\right] \Rightarrow \left[\overline{k}_n, \overline{k}_s\right];$		$\left.\left[\overline{\sigma}_c\right], \left[\overline{c}, \overline{\phi}\right] \Rightarrow \overline{\tau}_c \right\}$
radius multiplier	effective modulus stiffness ratio	friction coef.	effective modulus stiffness ratio		tensile and shear strength

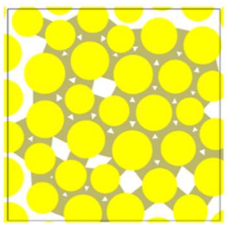

Figure 20 Primary parameters that define a parallel-bonded material.

Table 4 Parallel-Bonded Material Primary Parameters

Symbol	Name
Particle (disk/sphere)	
ρ	density
$\{D_l, D_u, \phi\}^{(j)}$	size distribution (min/max diameter, volume fraction)
Packing (linear model)	
P_m	material pressure (packing pressure)
α	local-damping factor (quasi-static conditions is 0.7)
$\{E_n^*, \kappa_n^*, \mu_n\}$	contacts during packing & after finalization
Ensemble	
χ	interaction-gap coefficient $(g_i = \chi d_{50})$
Parallel-bond model	
$\bar{\lambda}$	radius multiplier $\left(\bar{R} = \bar{\lambda} \min\left(R^{(1)}, R^{(2)}\right)\right)$
$\{E^*, \kappa^*, \mu\}$	effective modulus, stiffness ratio, friction coefficient
$\{\bar{E}^*, \bar{\kappa}^*\}$	bond effective modulus, bond stiffness ratio
$(\bar{\sigma}_c)_{\{\mathrm{m,sd}\}}$	tensile-strength distribution
$\bar{\gamma}$	cohesion to tensile strength ratio $(\bar{c} = \bar{\gamma}\, \bar{\sigma}_c)$
$\bar{\phi}$	friction angle

The full parameter set, of which the primary parameters are a subset, is given in Table 5. The properties in the parallel-bonded material group are used to set the relevant properties of the linear parallel bond model during material finalization, and the properties in the linear material group are assigned to particle-particle contacts during packing and that may form after material finalization.

The properties of the linear parallel bond model are as follows. The linear parallel bond model provides the behavior of two interfaces. The first interface is equivalent to the linear model, and the second interface is called a parallel bond.

- The properties of the first interface are listed in the linear group. The first interface provides linear and dashpot components. Only the linear component is active. The reference gap is zero but may be altered when a bond is installed. If a bond is installed and the contact gap is negative, then the reference gap is set equal to the contact gap at the time of bond installation (thereby establishing reference surfaces that are just touching and effectively removing the overlap such that there are no forces or moments in the material). The normal-force update mode is absolute. The normal and shear stiffnesses of the first interface are set based on a specified contact deformability (E^* and κ^* of the **deformability** method), and the friction coefficient is set to μ.

- The properties of the second interface are listed in the parallel-bond group. The second interface carries load only when it is bonded. Bonds are installed during material finalization at the particle-particle contacts with a gap less than or equal to the interaction gap (g_i). The normal and shear stiffnesses of the second interface are set based on a specified deformability ($\overline{E}^*$ and $\overline{\kappa}^*$ of the **pb_deformability** method). The remaining properties of the second interface correspond directly with properties in the parallel-bond group of the linear parallel bond contact model (ITASCA, 2026a, PFC – Contacts and Contact Models – Contact Models – Built-in Contact Models – Linear Parallel Bond Model).

The properties of the linear material group are as follows. The linear model provides linear and dashpot components. Only the linear component is active, the reference gap is zero and the normal-force update mode is absolute. The normal and shear stiffnesses are set based on a specified contact deformability ($E_n{}^*$ and $\kappa_n{}^*$ of the **deformability** method), and the friction coefficient is set to μ_n.

Table 5 Parallel-Bonded Material Parameters

Parameter	Type	Range	Default	Description
Material microproperties are listed via **`mpListMicroProps`**.				
Common material parameters are listed in Table 1 of Potyondy (2025).				
Packing parameters are listed in Table 9 of Potyondy (2025).				
Parallel-bonded material group				
Linear group				
E^*, **`pbm_emod`**	FLT	$[0.0, \infty)$	0.0	effective modulus
κ^*, **`pbm_krat`**	FLT	$[0.0, \infty)$	0.0	stiffness ratio
μ, **`pbm_fric`**	FLT	$[0.0, \infty)$	0.0	friction coefficient
Parallel-bond group				
g_i, **`pbm_igap`**	FLT	$[0.0, \infty)$	0.0	interaction gap

$\bar{\lambda}$, **pbm_rmul**	FLT	$(0.0,\infty)$	1.0	radius multiplier
$\bar{E}^*$, **pbm_bemod**	FLT	$[0.0,\infty)$	0.0	bond effective modulus
$\bar{\kappa}^*$, **pbm_bkrat**	FLT	$[0.0,\infty)$	1.0	bond stiffness ratio
$\bar{\beta}$, **pbm_mcf**	FLT	$[0.0,1.0]$	0.0	moment-contribution factor
$(\bar{\sigma}_c)_{\{m,sd\}}$ **pbm_ten_{m,sd}**	FLT	$[0.0,\infty)$	$\{0.0,0.0\}$	tensile-strength dist. [stress] (mean and std. deviation)
$(\bar{c})_{\{m,sd\}}$ **pbm_coh_{m,sd}**	FLT	$[0.0,\infty)$	$\{0.0,0.0\}$	cohesion dist. [stress] (mean and std. deviation)
$\bar{\gamma}$ **pbm_cohTenRatio**	FLT	$[0.0,\infty)$	0.0	cohesion to tensile strength ratio (At each contact, set $\bar{c} = \bar{\gamma}\,\bar{\sigma}_c$. If $\bar{\gamma} = 0.0$, then $(\bar{c})_{\{m,sd\}}$ is used.)
$\bar{\phi}$, **pbm_fa**	FLT	$[0.0,90.0)$	0.0	friction angle [degrees]
Linear material group (for particle-particle contacts during packing and that may form after material finalization)				
E_n^*, **lnm_emod**	FLT	$[0.0,\infty)$	0.0	effective modulus
κ_n^*, **lnm_krat**	FLT	$[0.0,\infty)$	0.0	stiffness ratio
μ_n, **lnm_fric**	FLT	$[0.0,\infty)$	0.0	friction coefficient

2.3 Material Microproperties

We denote our base material as the TB material and produce three TB materials that differ only in their median particle sizes of 50, 100, and 200 microns. The three materials are designated as TB50, TB100 and TB200. The specimen size is chosen large enough to obtain a representative volume meaning that the macroscopic properties will remain the same for larger specimens.[18] The primary microproperties of the base material are listed in Table 6 while the full set of microproperties is listed in Table 7. The material is shown in Figure 21.

[18] This will need to be confirmed by increasing the specimen size and rerunning the laboratory tests. The process is like what was done in Potyondy (2019b, Section 2.4.2 Size Effect).

Table 6 Primary Microproperties of TB Materials[a]

Packing (linear model)

P_m (MPa)	E_n^* (GPa)	κ_n^*	μ_n
500	6	2.7	0.5

Ensemble

χ
0

Parallel-bond model (1)

$\bar{\lambda}$	E^* (GPa)	κ^*	μ
1	6	2.7	0.5

Parallel-bond model (2)

$\bar{E}^*$ (GPa)	$\bar{\kappa}^*$	$(\bar{\sigma}_c)^b$	$\bar{\gamma}$	$\bar{\phi}$ (deg)
6	2.7	$\{4,0\}$	3	0

[a] $\left[\text{TB}\{50,100,200\}\right] \Leftrightarrow \left[d_{50} = \{50,100,200\}\ \mu\text{m}\right]$

[b] mean & standard deviation (units: MPa)

Table 7 Microproperties of TB Materials

Property	Value
Common group	
N_m	$\text{TB}\{50,100,200\}$
$T_m,\ \alpha,\ C_\rho,\ \rho_v\ [\text{kg/m}^3]$	$2,\ 0.7,\ 1,\ 2270$
$S_g,\ T_{SD},\ \{D_{\{l,u\}}\,[\mu\text{m}],\ \phi\},\ D_{mult}$	$0,\ 0,\ \{40.0, 60.0, 1.0\},\ \begin{cases} 1.0 & \text{TB50} \\ 2.0 & \text{TB100} \\ 4.0 & \text{TB200} \end{cases}$
Packing group	
$S_{RN},\ P_m\,[\text{MPa}],\ \varepsilon_P,\ \varepsilon_{\lim},\ n_{\lim}$	$10000,\ 500.0,\ 1\times10^{-2},\ 8\times10^{-3},\ 2\times10^{6}$
$C_p,\ n_c$	$1,\ 0.04$
Parallel-bonded material group	
Linear group	
$E^*\,[\text{GPa}],\ \kappa^*,\ \mu$	$6.0,\ 2.7,\ 0.5$

Parallel-bond group	
$g_i\,[\mu\text{m}],\ \bar{\lambda},\ \bar{E}^*\,[\text{GPa}],\ \bar{\kappa}^*,\ \bar{\beta}$	$0,\ 1,\ 6.0,\ 2.7,\ 1$
$(\bar{\sigma}_c)_{\{\text{m, sd}\}}\,[\text{MPa}],\ (\bar{c})_{\{\text{m, sd}\}}\,[\text{MPa}],\ \bar{\phi}\,[\text{degrees}]$	$\{4.0,0\},\ \{12.0,0\},\ 0$
Linear material group	
$E_n^*\,[\text{GPa}],\ \kappa_n^*,\ \mu_n$	$6.0,\ 2.7,\ 0.5$

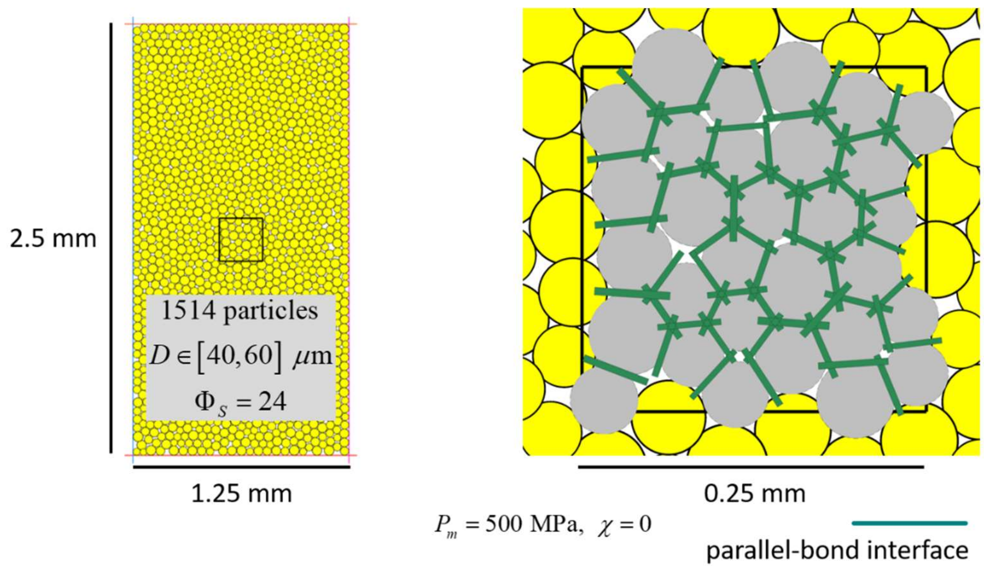

Figure 21 TB50 material at the end of material genesis showing specimen and intact parallel bonds in the microstructural box.

2.4 Material Response (Lab and Cutting Tests)

The Torry Buff material is described in Section 3.4 of Potyondy and Blanksma (2015). The following properties are typical of Torrey Buff sandstone: density of $2270\ \text{kg/m}^3$; nominal grain size of 50 microns; Brazilian strength (σ_B) of 3.6 MPa; unconfined-compressive strength (σ_{UCS}) of 58 MPa; and Young's modulus in compression (E_c) and Poisson's ratio in compression (ν_c) (measured during unconfined-compression test) of 10.5 GPa and 0.23, respectively.

2.4.1 Lab Tests

The lab-testing capability is provided in the **`mg_labTests`** example-project directory.

The base material has the following properties:[19] direct-tension strength (σ_t) of 3.3 MPa (see Figure 22);[20] unconfined-compressive strength (σ_{UCS}) of 22 MPa, effective Young's modulus and Poisson's ratio[21] in compression $(E'_c \text{ and } \nu'_c)$ of 12.4 GPa and 0.26, respectively (see Figure 23); and peak axial stress for confinement of 3 MPa (σ_{f3}) of 41 MPa. It is expected that PFC2D and PFC3D flat-jointed materials could be calibrated to match σ_t, σ_{UCS}, E_c, and σ_{f3} of Torry Buff sandstone.

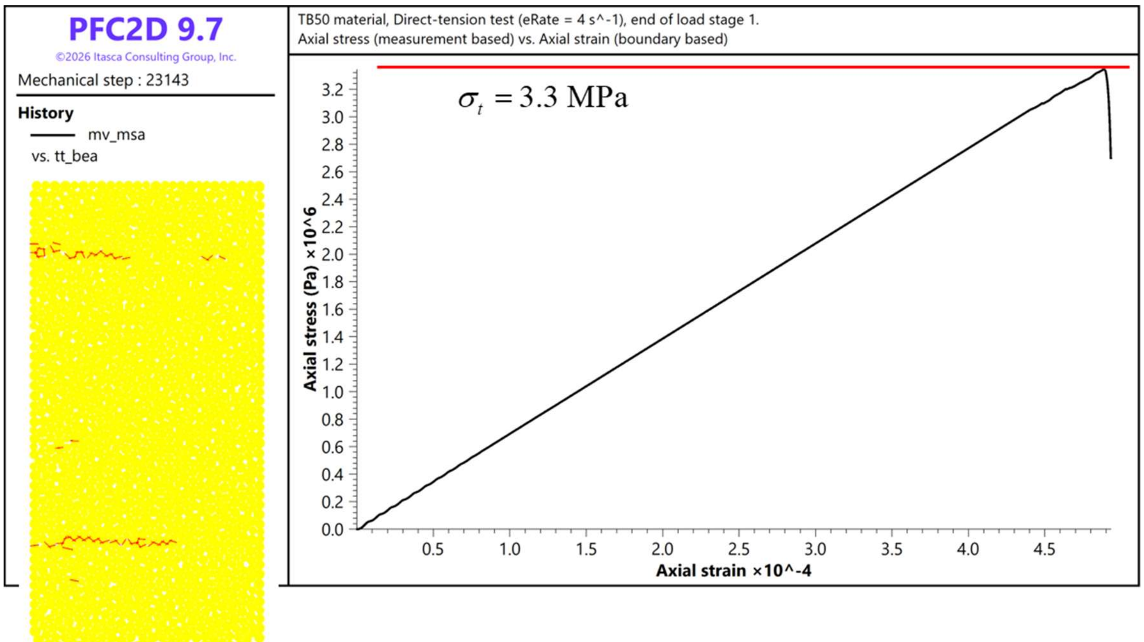

Figure 22 Tensile-test response of TB50 base material.

[19] The loading rate for the models described here is just above the upper limit of being quasistatic such that the peak stresses may be a few percent higher than their quasistatic values. The current loading rate should be sufficient for purposes of model development and calibration. The final models should be rerun at a reduced loading rate that is quasistatic.

[20] Direct-tension strengths can be converted to Brazilian strengths by dividing them by approximately 0.8.

[21] The Young's modulus and Poisson's ratio obtained from a PFC2D biaxial test are effective because the PFC2D material consists of unit-thickness disks and cannot be related directly to a linear elastic isotropic continuum material (Potyondy, 2025, Section 7.1 Measuring Elastic Constants).

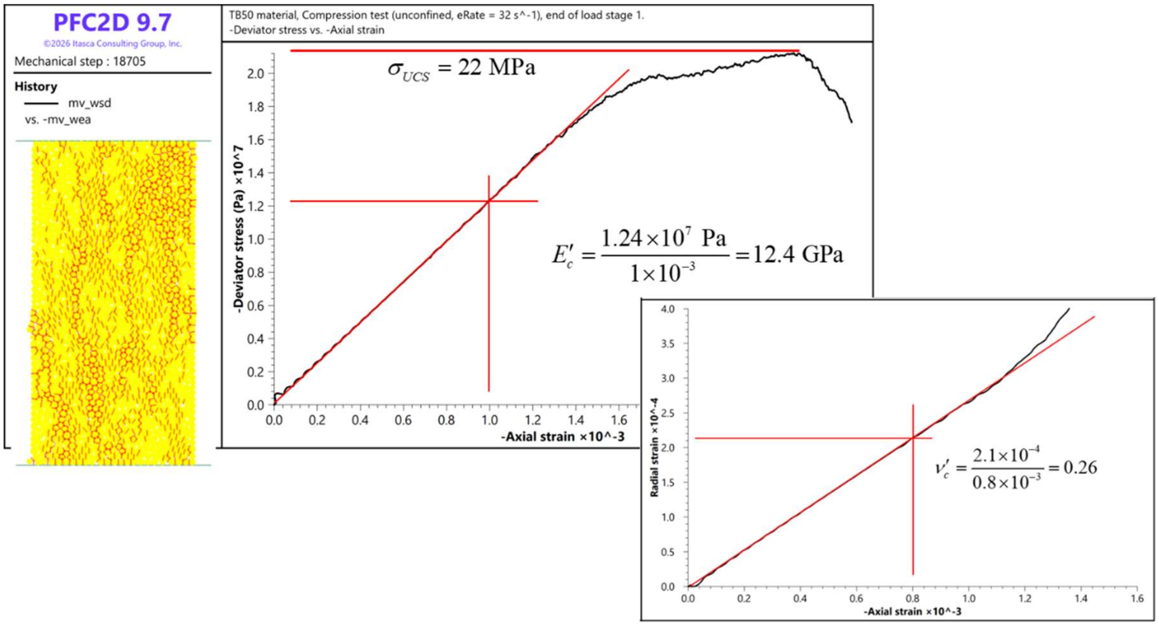

Figure 23 UCS-test response of TB50 base material.

2.4.2 Cutting Tests

The cutting-test capability is provided in the **mg_cutTest** example-project directory. The example serves as a base case and provides a cutter-rock model at the lowest resolution sufficient to demonstrate system behavior. This section describes the modeling capability in terms of the model components, how to visualize damaged microstructure, and the plots. The physics revealed by the modeling is discussed in the following section.

A rectangular (4.0 mm high, 12.0 mm wide) and unit-thickness specimen of the TB200 material with an average grain diameter of 200 microns is created. The cutting-test properties are listed in Table 8. Dry and wet (5-MPa confining pressure) cutting tests are performed. The initial model is shown in Figure 24, and the damaged microstructures after 3 mm of cutter displacement are shown in Figures 25 and 26. An alternate means of displaying the damaged microstructure is shown in Figure 27.

Table 8 Base-Case Cutting Test Properties

Property	Value
Geometry, position and orientation group:	
n_c,	2
$n_f^{(1)}$, $(\mathbf{c}'_i)^{(1)}$ [mm]	5, $\left\{ \begin{matrix} (-1.576,3.5),(-1.576,0),(0,0),(0.4243,0.4243), \\ (0.4243,3.5),(-1.576,3.5) \end{matrix} \right\}$
$n_f^{(2)}$, $(\mathbf{c}'_i)^{(2)}$ [mm]	5, $\left\{ \begin{matrix} (-1.576,3.5),(-1.576,0),(0,0),(0.4243,0.4243), \\ (0.4243,3.5),(-1.576,3.5) \end{matrix} \right\}$

$\{\theta_r\,[\text{deg.}],\ D\,[\text{mm}],\ o_c\,[\text{mm}],\ (A_c)_{3D}\,[\text{mm}^2]\}^{(1)}$	$20,\ 1,\ 0.81,\ \{5.39\}^1$
$\{\theta_r\,[\text{deg.}],\ D\,[\text{mm}],\ o_c\,[\text{mm}],\ (A_c)_{3D}\,[\text{mm}^2]\}^{(2)}$	$10,\ 2,\ 3.2,\ \{5.27\}^2$
Boundary and initial conditions group:	
$t_g\,[\mu\text{m}],\ \alpha_c,\ V^{(1)}\,[\text{mm/s}],\ V^{(2)}\,[\text{mm/s}]$	$\begin{cases} 200,\ \text{TB200} \\ 100,\ \text{TB100},\ 0.02,\ 100,\ 90 \\ 100,\ \text{TB50} \end{cases}$
Material properties group:	
$\{E_c^*\,[\text{GPa}],\ \kappa_c^*,\ \mu_c\}^{(1,2)}$	$\{6,\ 2,\ 0.5\}$
Chaining-algorithm group:	
$B_c,\ B_s,\ P\,[\text{MPa}],\ f_b^{(1)},\ f_b^{(2)}$	$\begin{cases} \text{false, dry cut} \\ \text{true, wet cut} \end{cases},\ \text{both},\ \{1,5,50\},\ 1,\ 1$
$g\,[\mu\text{m}],\ N_c,\ \varepsilon_{\text{lim}},\ n_{\text{lim}}$	$0.2\tilde{D}_g = \begin{cases} 40,\ \text{TB200} \\ 20,\ \text{TB100},\ 500,\ 1\times10^{-5},\ 1\times10^{6} \\ 10,\ \text{TB50} \end{cases}$
Control and monitoring group:	
$M_d,\ R_h,\ R_E,\ o_v\,[\text{mm}],\ R_v,\ R_{\text{ps}},\ g_f\,[\mu\text{m}],\ R_c$	$\text{false},\ 100,\ 100,\ 3,\ 1000,\ 1\times10^{6},\ 50,\ 1\times10^{6}$

1 SiPlan Test: DOC = 1 mm, rake angle = 20 degrees (Blanksma and Potyondy, 2015).
2 SiPlan Test: DOC = 1 mm, rake angle = 10 degrees (Blanksma and Potyondy, 2015).

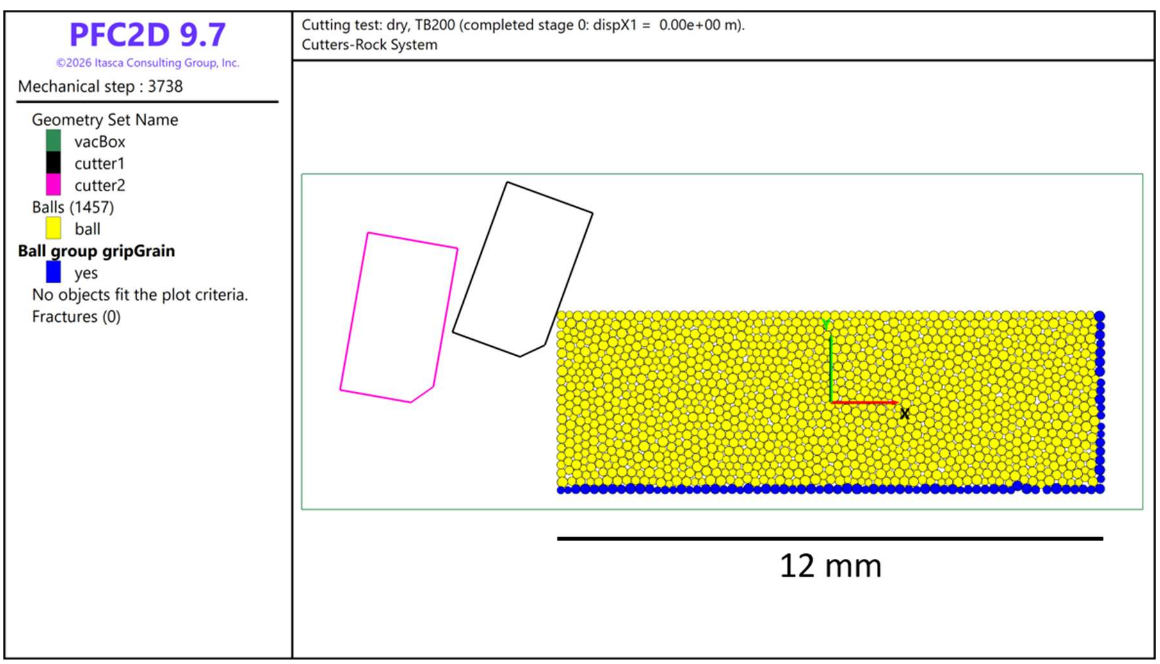

Figure 24 Initial base case cutting-test model showing vacuum box, cutters, specimen, grip grains, and origin of global coordinate system.

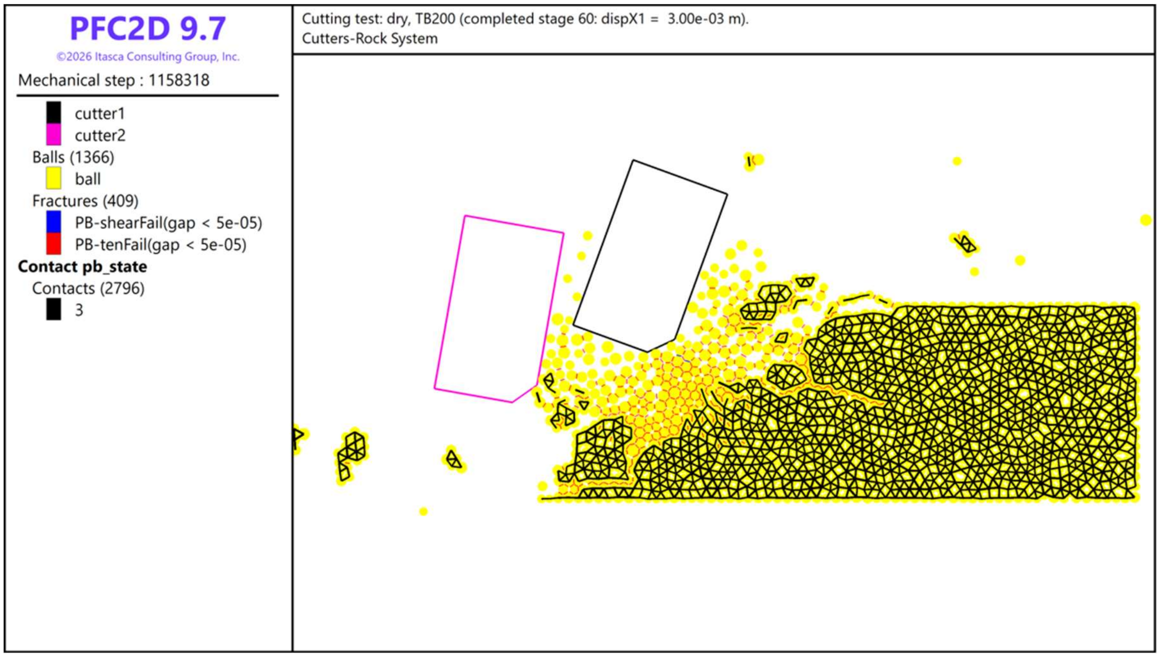

Figure 25 ***Base case dry cutting-test model after 3 mm of cutter-1 displacement showing grains, intact parallel bonds, and cracks with gap less than 50 microns (50% size).***

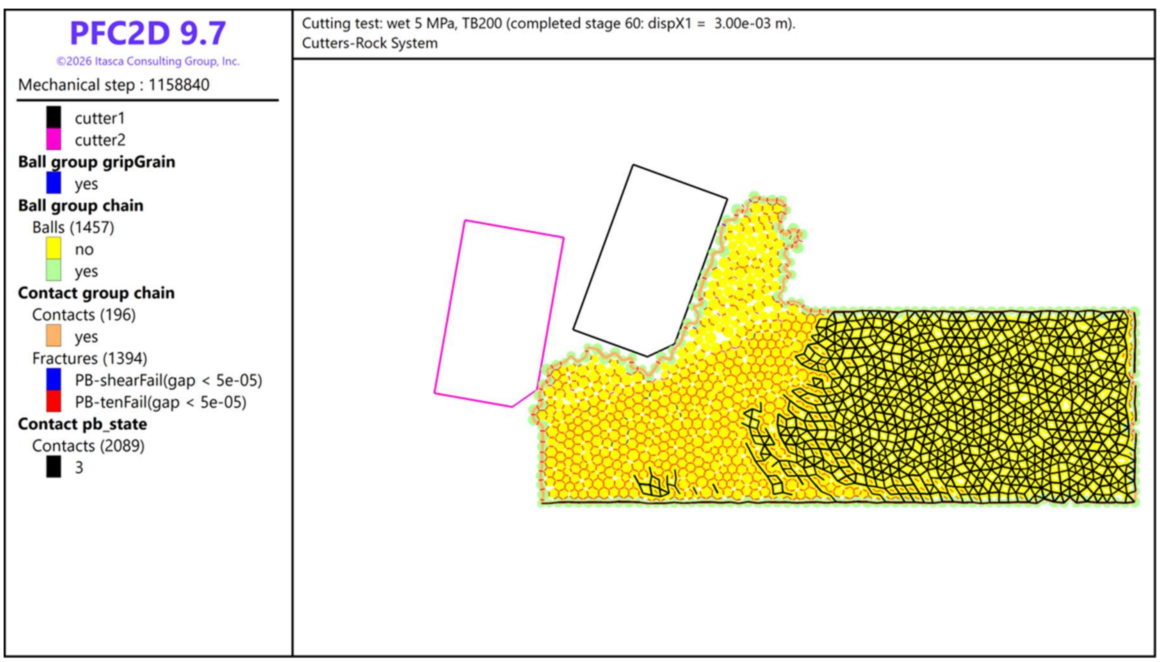

Figure 26 ***Base case wet cutting-test model after 3 mm of cutter-1 displacement showing pressure-application chain, grains, intact parallel bonds, and cracks with gap less than 50 microns (50% size).***

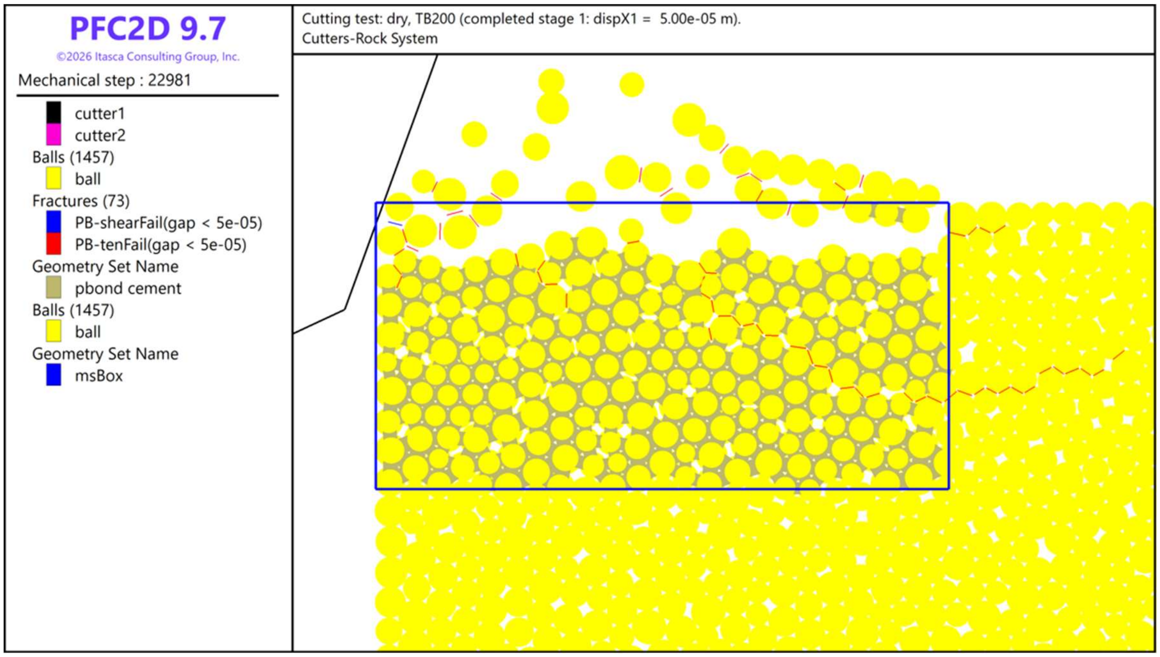

Figure 27 ***Base case dry cutting-test model after 50 microns of cutter-1 displacement showing in the blue microstructural box: grains (yellow disks, 80% size), intact parallel bonds (tan cylinders, 50% size), and cracks with gap less than 50 microns (50% size).***

The rock-cutting package provides plots to visualize and interact with the model. The title bar at the top of each plot contains the test name (**`rc_testName`**), material name (**`cm_matName`**), and test stage with associated cutter-1 displacement (dispX1) as well as a description of the plot itself in the second line. The line-chart labels assume that the model uses SI units (e.g., stress is labelled as having units of Pascals). The plots include the following — it is straightforward to create other plots; these plots are essential to model use and interpretation.

- **`cuttersRock`** The model can be visualized as demonstrated in the four preceding figures.
- **`forceXY_dispX1`** A line chart of cutter force versus cutter-1 displacement is provided (see Figure 28).
- **`forceAvgXY_dispX1`** A line chart of average cutter force versus cutter-1 displacement is provided (see Figure 29).
- **`ck_dispX1`** A line chart of cracks versus cutter-1 displacement is provided (see Figure 30).
- **`energies_dispX1`** A line chart of energy quantities versus cutter-1 displacement is provided (see Figure 31). A line chart of energy quantities versus cutting time is provided in the plot **`energies_cutTime`**.

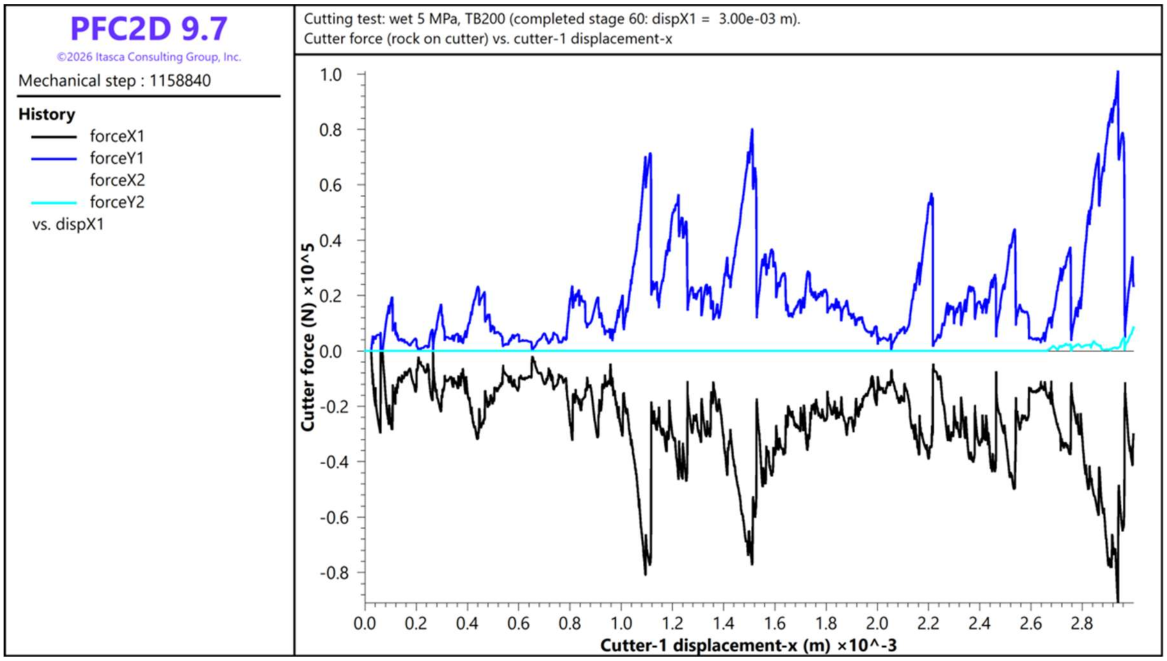

Figure 28 ***Plot*** **`forceXY_dispX1`** ***(wet model).***

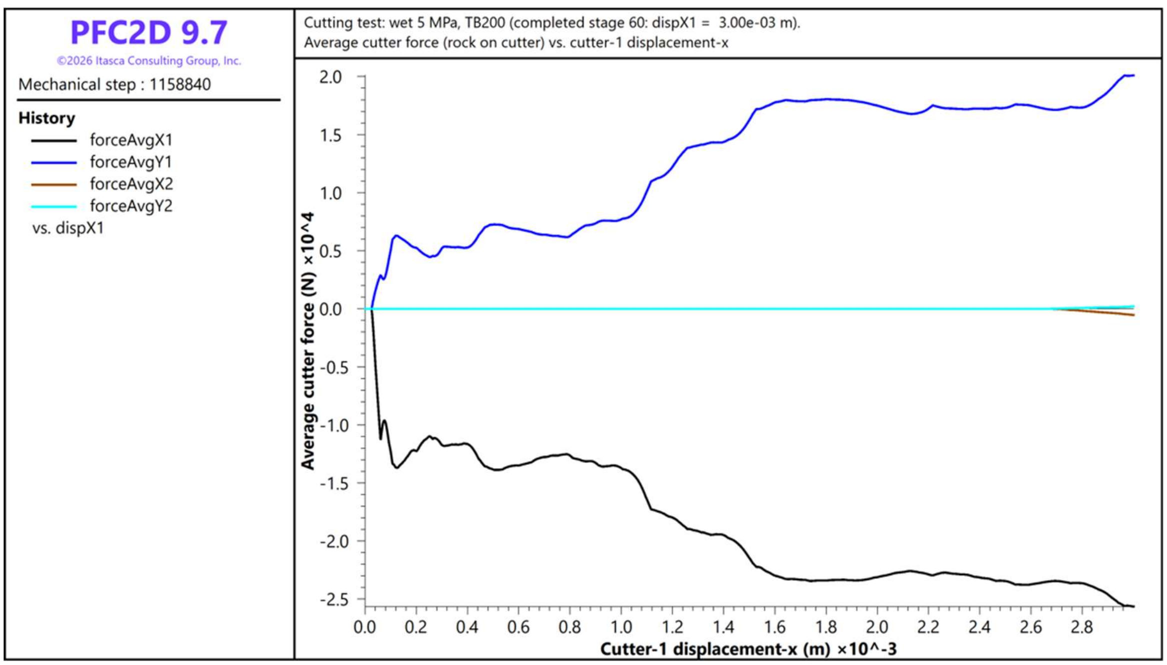

Figure 29 ***Plot*** **`forceAvgXY_dispX1`** ***(wet model).***

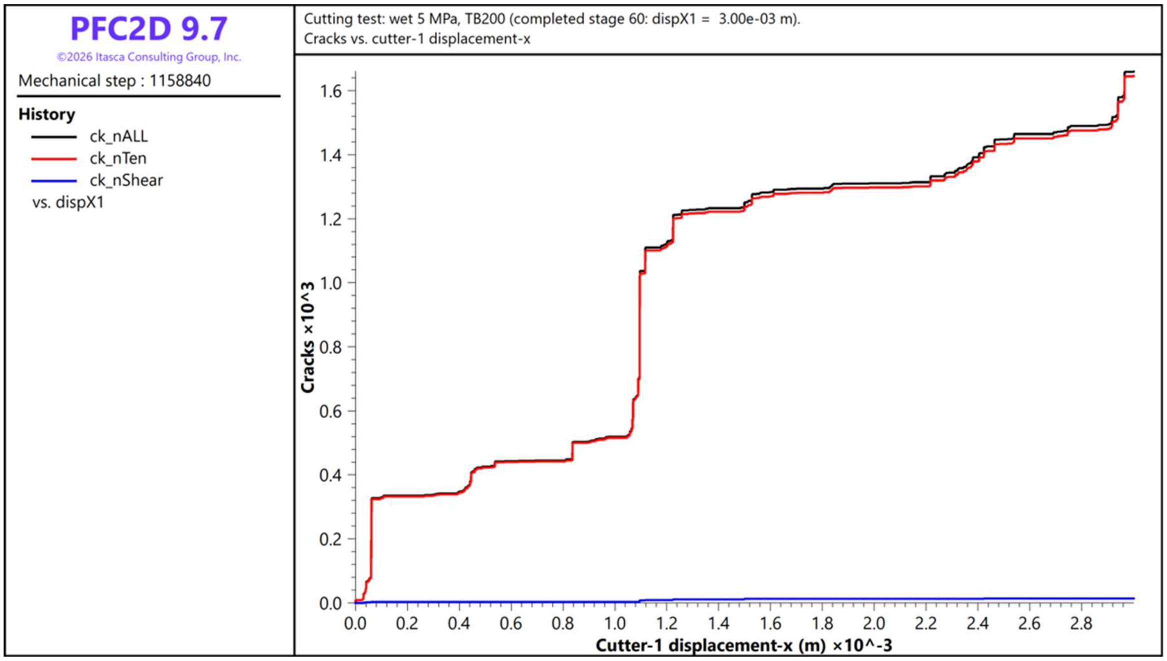

Figure 30 ***Plot*** `ck_dispX1` ***(wet model).***

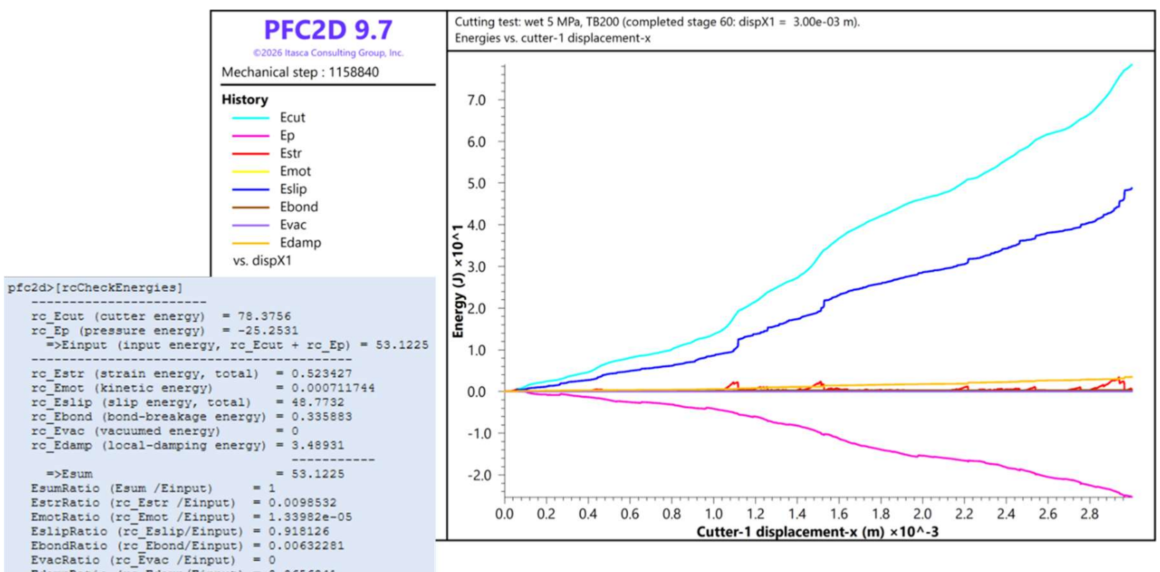

Figure 31 ***Plot*** `energies_dispX1` ***(wet model).***

2.4.3 Cutting Tests with Version 6

The cutting tests described here were performed with PFC2D version 6. This material is taken from Potyondy (2019a) and is included here for completeness. It is expected that these results will also be reproduced by the rock-cutting package (**`rcPkg9.N`**) that works with PFC2D version 9.

2.4.3.1 Dry cutting only — no chain seals

This example serves as a dry-cutting base case and provides a cutter-rock model at the lowest resolution sufficient to demonstrate system behavior.

A rectangular (4.0 mm high, 12.0 mm wide) and unit-thickness specimen of the TB200 material with an average grain diameter of 200 microns is created. The cutting-test properties are listed in Table 8. The initial cutter-rock system is shown in Figure 32, the initial damage is shown in Figure 33, and the cutter-rock system after 8 mm of cutter displacement is shown in Figures 34 and 35. The cutter forces (both absolute and displacement-averaged) and mechanical specific energies are plotted versus cutter displacement in Figures 36–38, and the energy quantities are plotted versus cutting time in Figure 39.

The force-chain fabric (Potyondy [2025, section Force Chain Fabric]) during initial cutter-rock engagement is shown in Figures 40 and 41. The cutter-rock system behavior consists of repeated episodes of cutter force build-up followed by bond breakage and stress redistribution during which the cutter force drops to zero. The cutter-rock systems of the TB100 and TB50 materials after 8 mm of cutter displacement are shown in Figures 42 and 43.

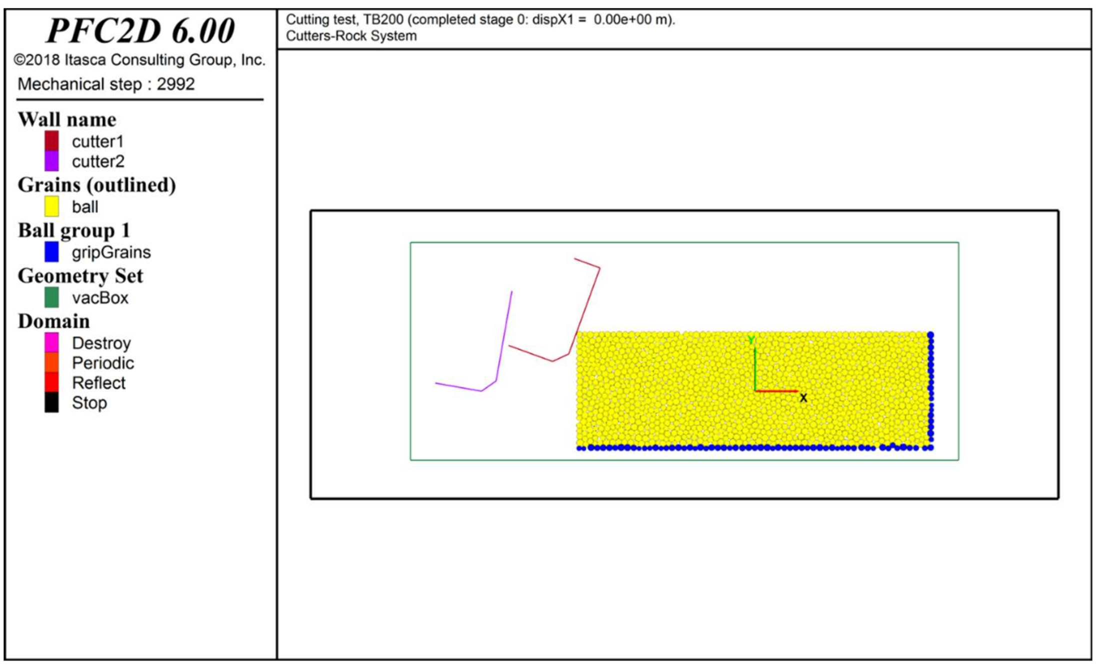

Figure 32 ***Initial base case cutting-test model showing domain, vacuum box, cutters, specimen, grip grains, and origin of global coordinate system.***

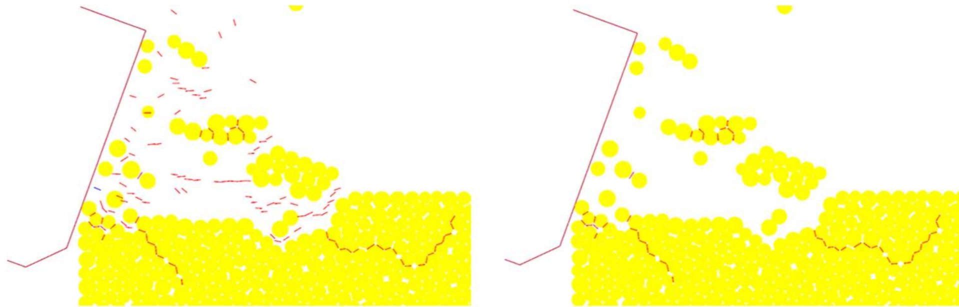

Figure 33 ***Base case cutting-test model after 0.1 mm of cutter-1 displacement showing cutter, grains at true size and cracks (all and filtered, with failure mode: red/blue = tensile/shear).***

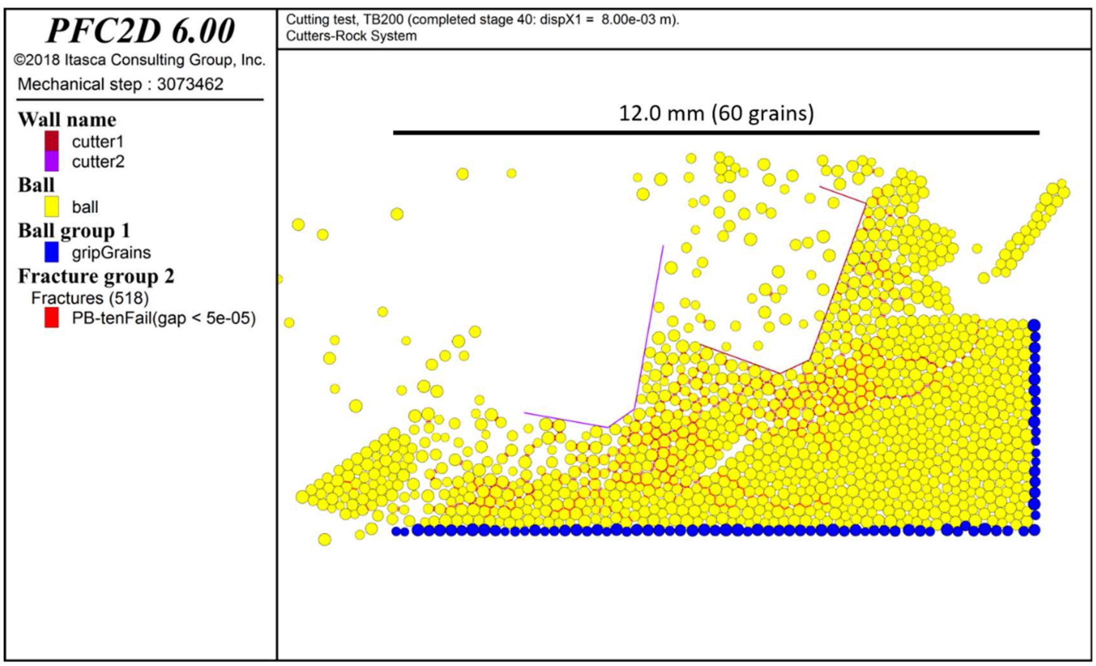

Figure 34 ***Base case cutting-test model after 8 mm of cutter-1 displacement showing grains and filtered cracks with gap less than 50 microns (50% size).***

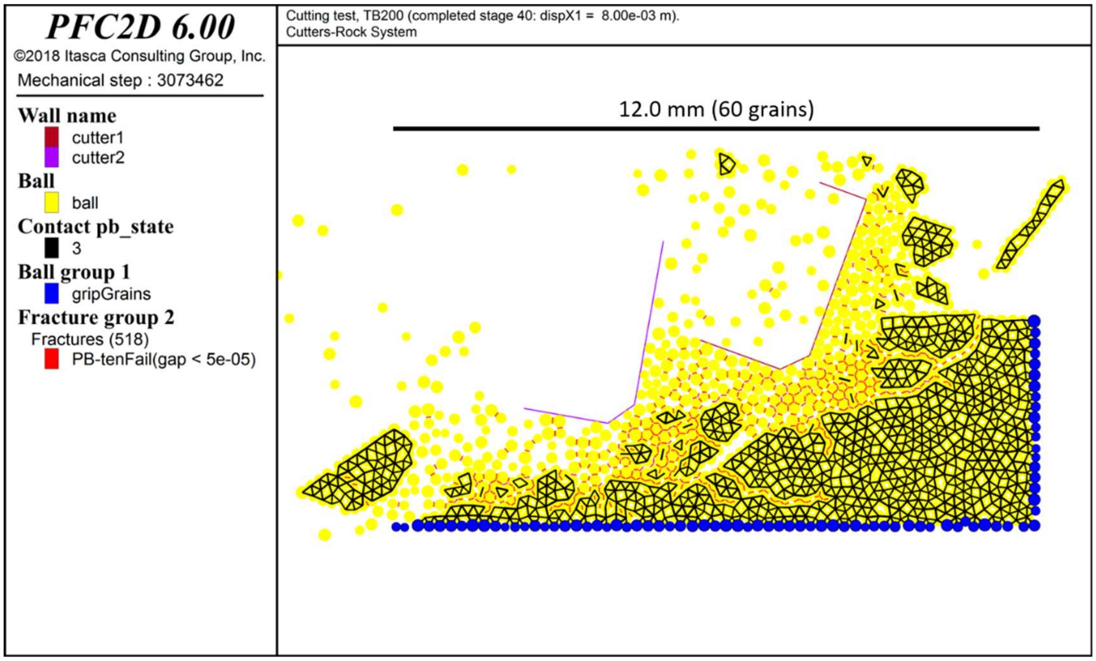

Figure 35 ***Base case cutting-test model after 8 mm of cutter-1 displacement showing grains, intact parallel bonds, and filtered cracks with gap less than 50 microns (50% size).***

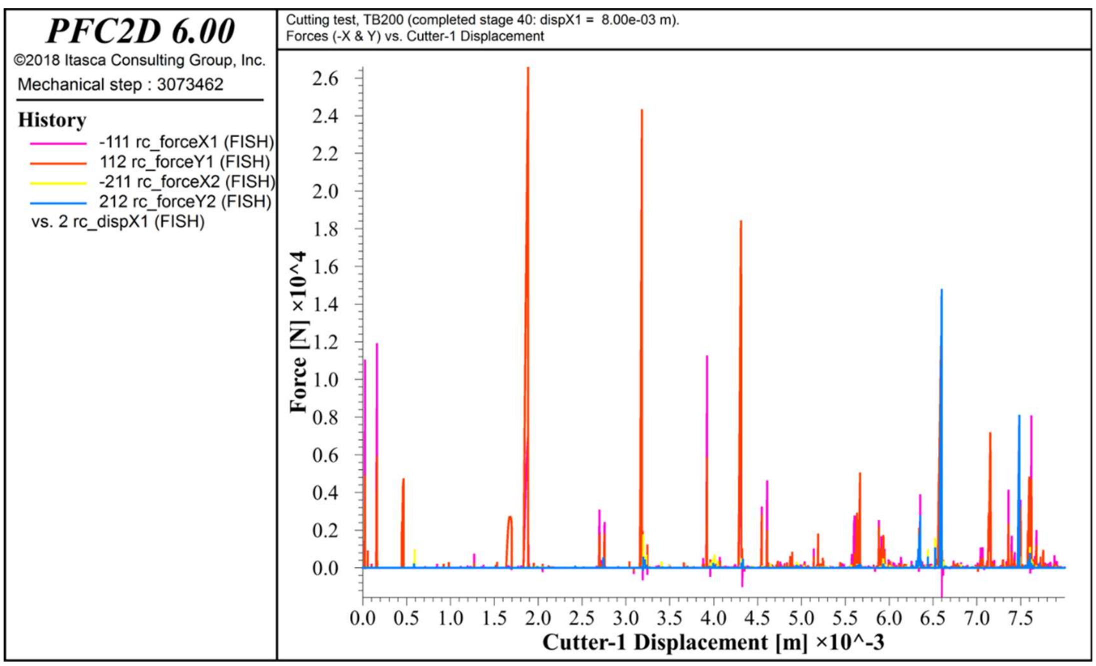

Figure 36 ***Cutter forces versus cutter-1 displacement for the base case cutting-test model.***

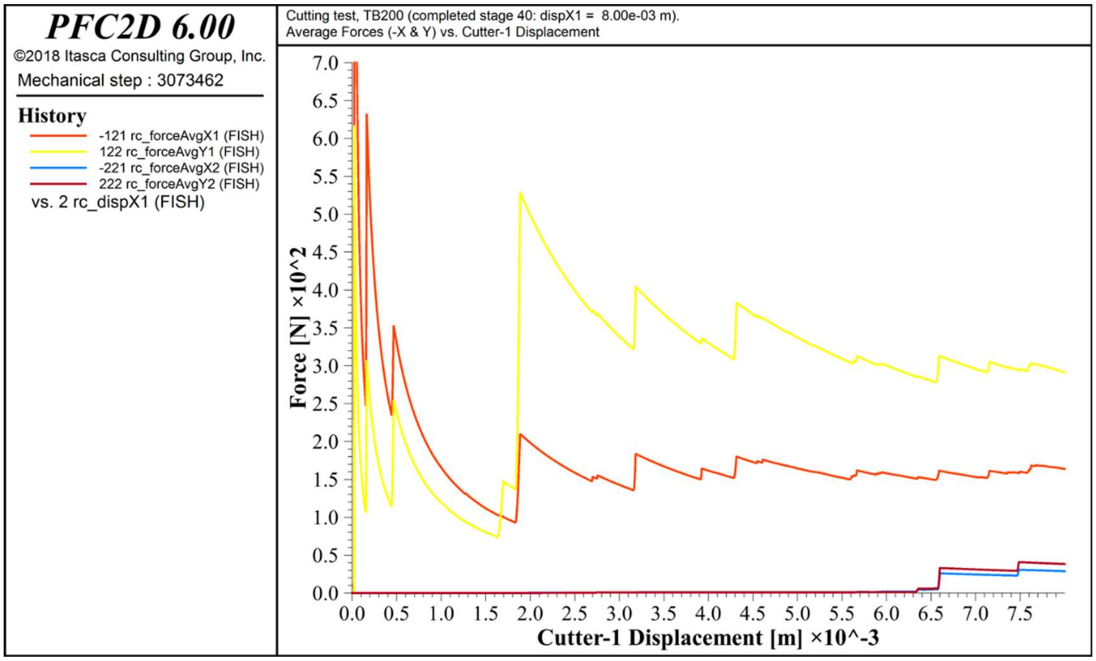

Figure 37 ***Displacement-averaged cutter forces versus cutter-1 displacement for the base case cutting-test model.***

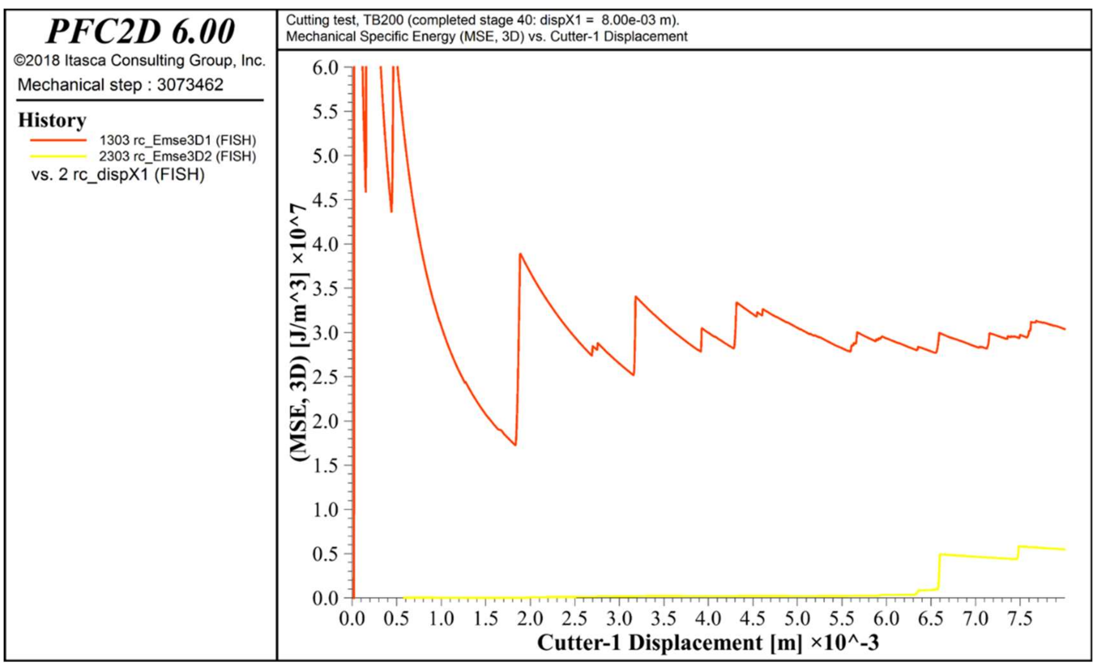

Figure 38 ***Mechanical specific energies (MSE, 3D) versus cutter-1 displacement for the base case cutting-test model.***

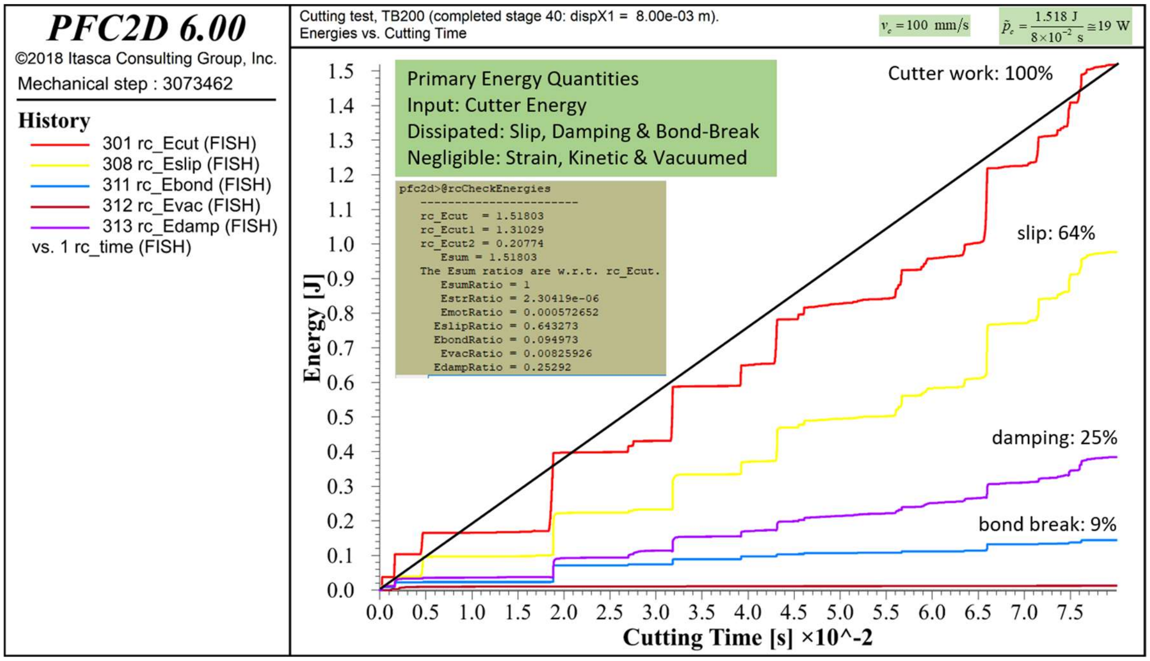

Figure 39 ***Energies versus cutting time for the base case cutting-test model.***

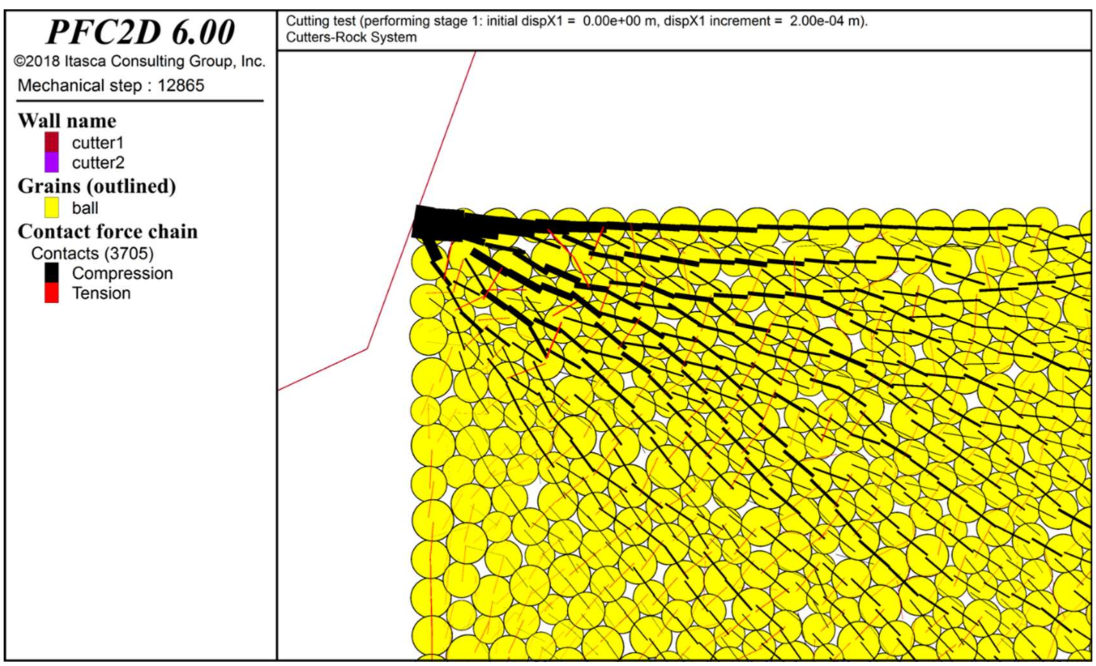

Figure 40 ***Force-chain fabric (bi-colored: compression and tension) during initial cutter-rock engagement in the base case cutting-test model.***

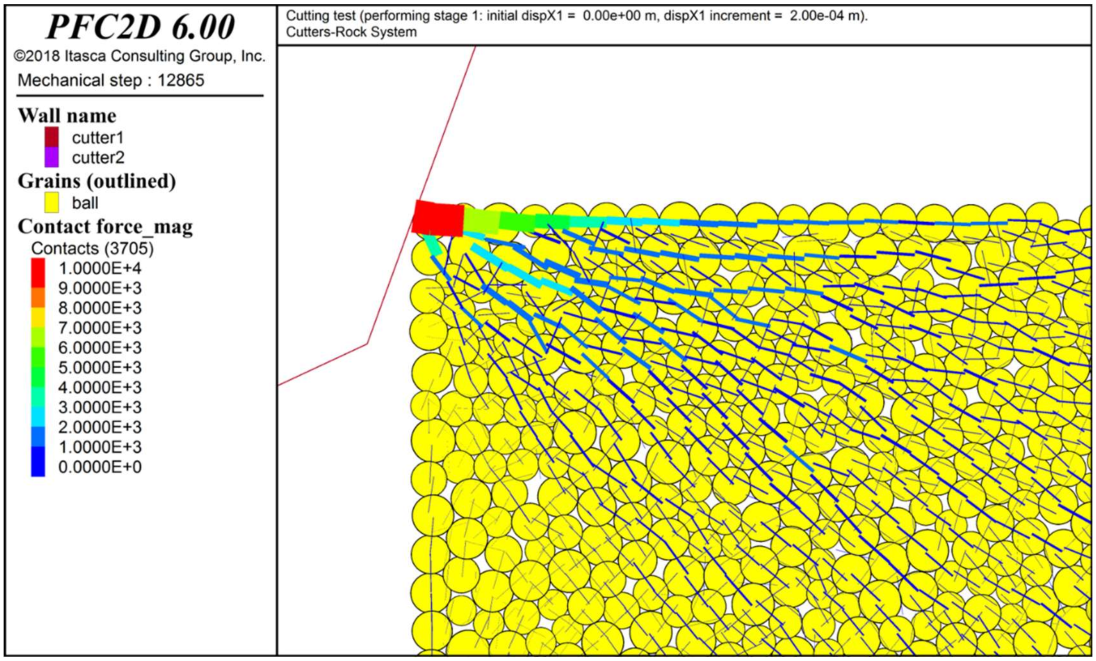

Figure 41 Force-chain fabric (scale-colored: magnitude) during initial cutter-rock engagement in the base case cutting-test model.

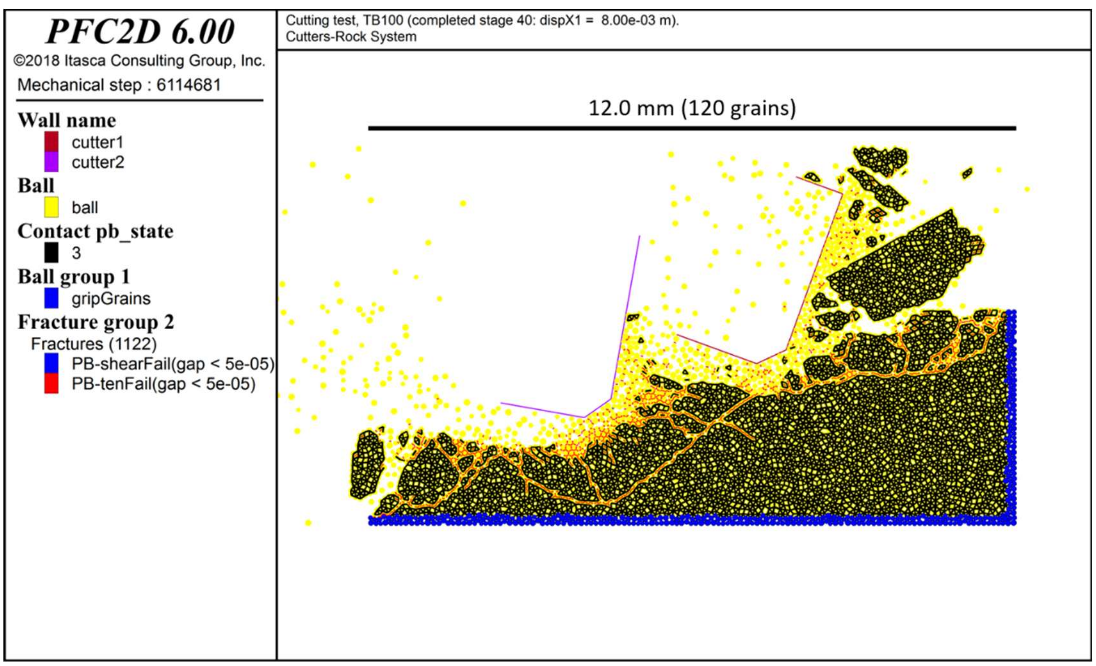

Figure 42 Base case cutting-test model of the TB100 material after 8 mm of cutter-1 displacement showing grains, intact parallel bonds, and filtered cracks with gap less than 50 microns.

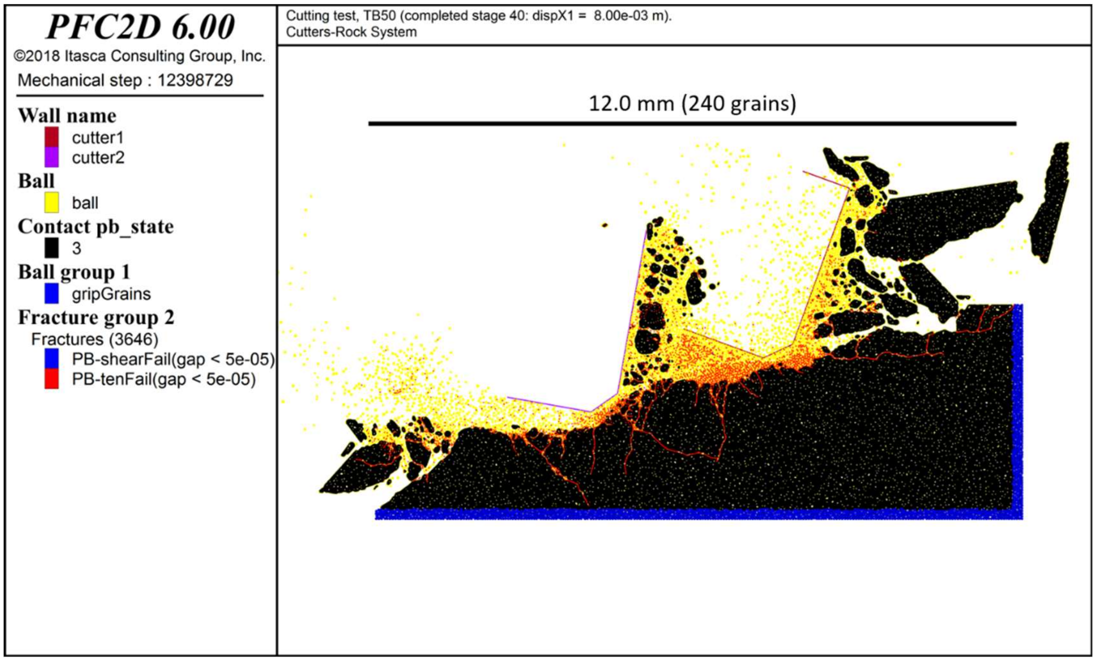

Figure 43 Base case cutting-test model of the TB50 material after 8 mm of cutter-1 displacement showing grains, intact parallel bonds, and filtered cracks with gap less than 50 microns.

2.4.3.2 Dry and wet cutting — no chain seals

The present example performs both dry and wet cutting on the material with a grain size equal to that of Torrey Buff sandstone, with wet-cutting pressures of 1 and 5 MPa. A rectangular (4.0 mm high, 12.0 mm wide) and unit-thickness specimen of the TB50 material with an average grain diameter of 50 microns is created. The material microproperties and cutting-test properties are listed in the previous section. Animations (in the form of MP4 files) are provided on the USB stick that accompanies Potyondy (2019a). The animations include plots of specimen damage, layer deformation, and force-chain evolution.

The damage evolution for the dry- and wet-cutting tests is shown in Figures 44–46. The response is brittle for the dry-cutting test with relatively large fragments forming in front of cutter-1 and smaller fragments flowing beneath the cutter. There are a few large fractures beneath the fragmented layer. The response is ductile for the wet-cutting tests with a mass of broken material (consisting of grains with all bonds broken) forming in front of cutter-1, moving up the cutter face and flowing beneath the cutter. The heavily damaged layer beneath the cutter is approximately 10 grains thick for the 1-MPa confinement case. There is additional fracturing (consisting of fingers of broken material extending downward at approximately 45 degrees from the horizontal) beneath this layer, and the fracturing is more intense for the 5-MPa confinement case.

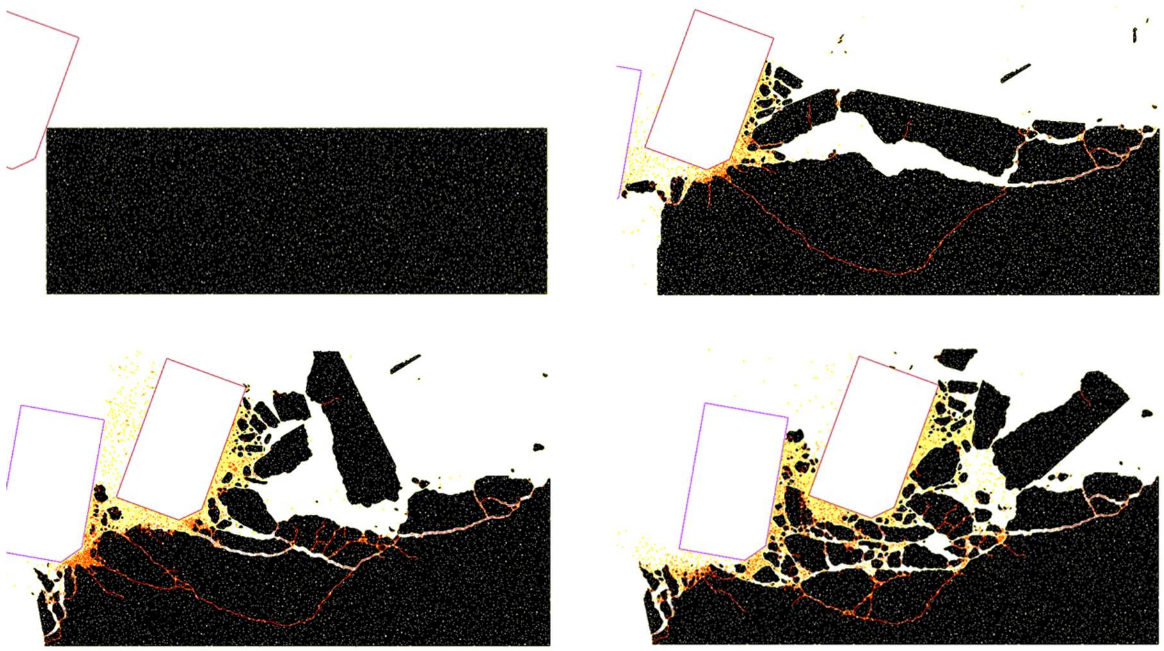

Figure 44 Damage evolution during dry cutting of the TB50 material for cutter-1 displacements of 0, 2, 4, and 6 mm.

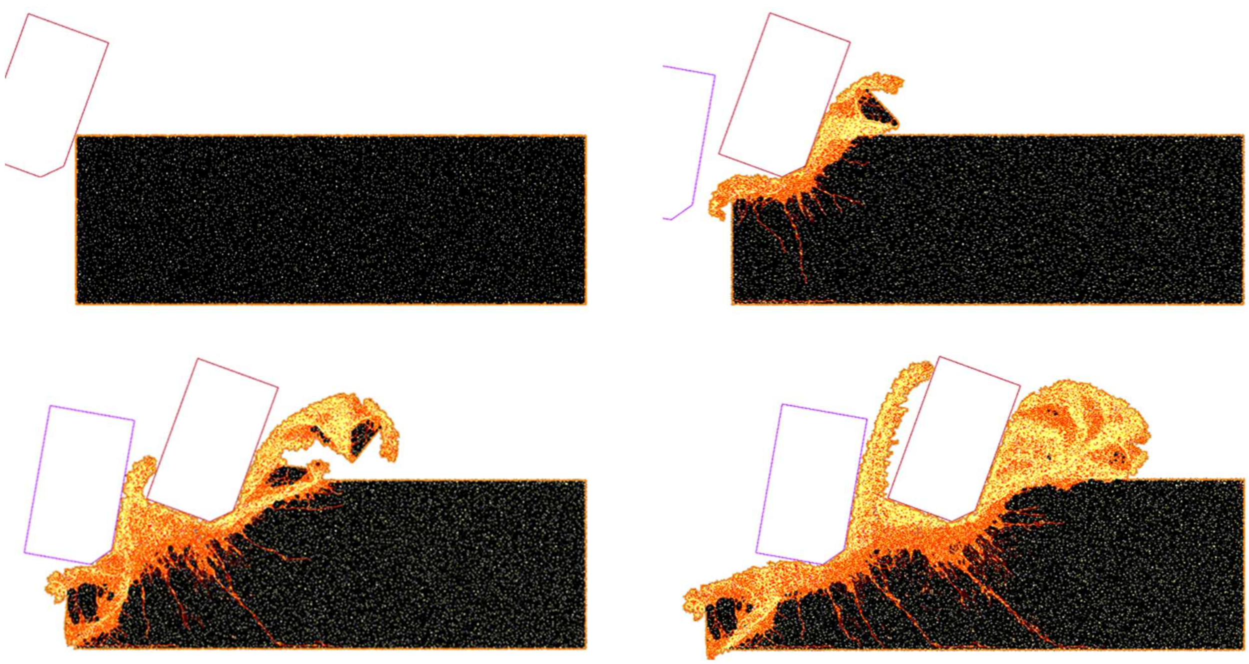

Figure 45 Damage evolution during wet cutting of the TB50 material subjected to 1-MPa confinement for cutter-1 displacements of 0, 2, 4, and 6 mm.

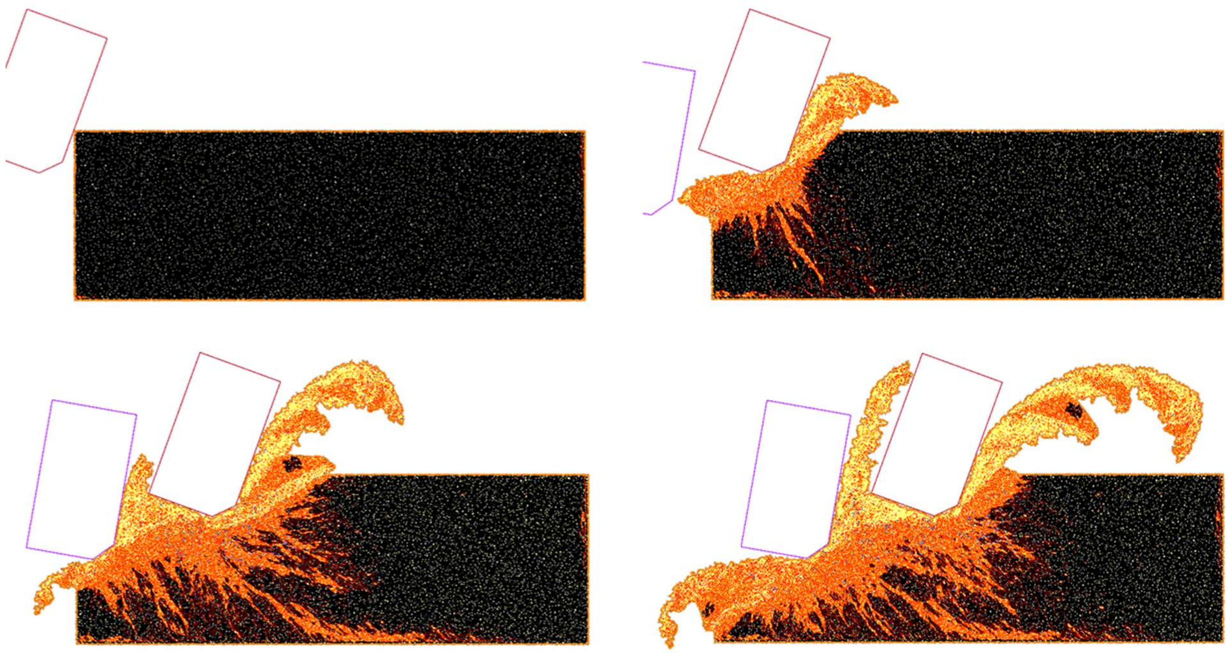

Figure 46 Damage evolution during wet cutting of the TB50 material subjected to 5-MPa confinement for cutter-1 displacements of 0, 2, 4, and 6 mm.

The material deformation field for the dry- and wet-cutting tests is shown in Figures 47–49, in which horizontal layers of two-grain thickness have been marked onto the initial model. The large fragments that form in front of cutter-1 and are subsequently broken into smaller fragments during dry cutting are clearly seen in Figure 47. The deformation during wet cutting consists of horizontal layers of material being sheared off and then riding up the face of cutter-1 (see the lower-left images for both wet-cutting cases and Figure 50). As the broken material rides up the cutter face, it bends forward and eventually contacts the front surface, forming a globular mass of broken material. The cutting does not remain in contact with the cutter face; instead, the mud pressure acts between the cutter and rock, which forces the cutting to bend forward. A modification to the chaining algorithm that identifies a sealed region along each cutter over which no pressure acts has been implemented, and animations showing behavior with and without chain seals are provided on the USB stick that accompanies this memo. The sealing scheme forces the cutting to remain in intimate contact with the cutter face as it is forced upward; however, preliminary study of the animations suggests that it does not substantially alter the wet-cutting deformation mechanism of the model. Further study of the animations is warranted.

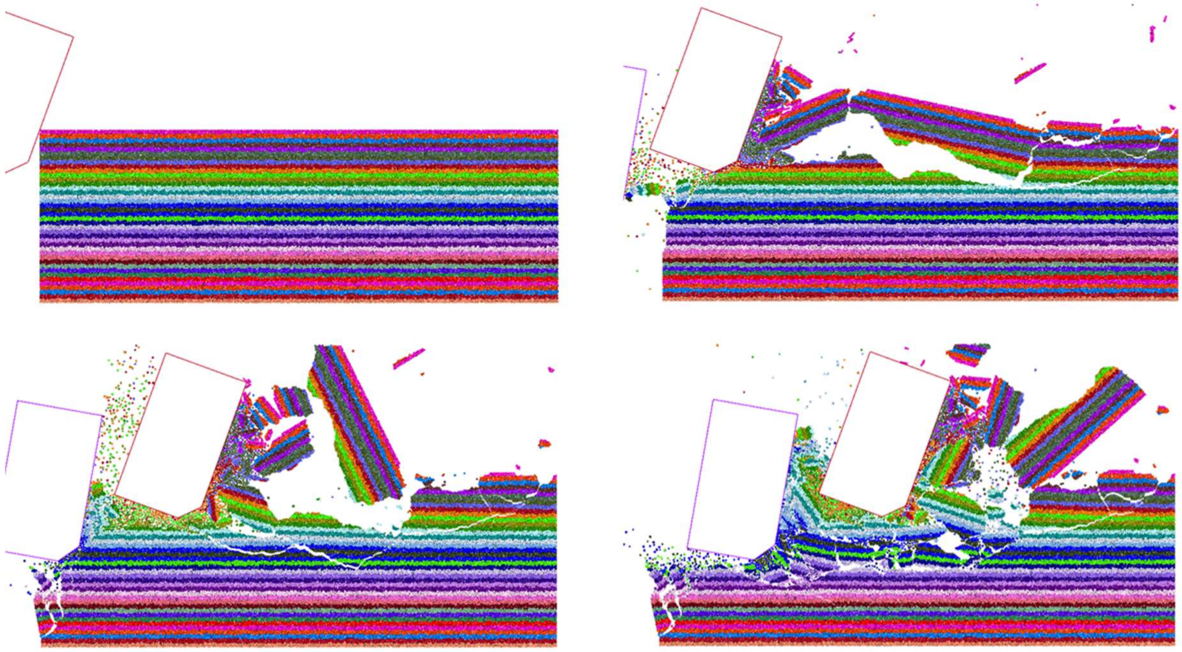

Figure 47 ***Material deformation during dry cutting of the TB50 material for cutter-1 displacements of 0, 2, 4, and 6 mm.***

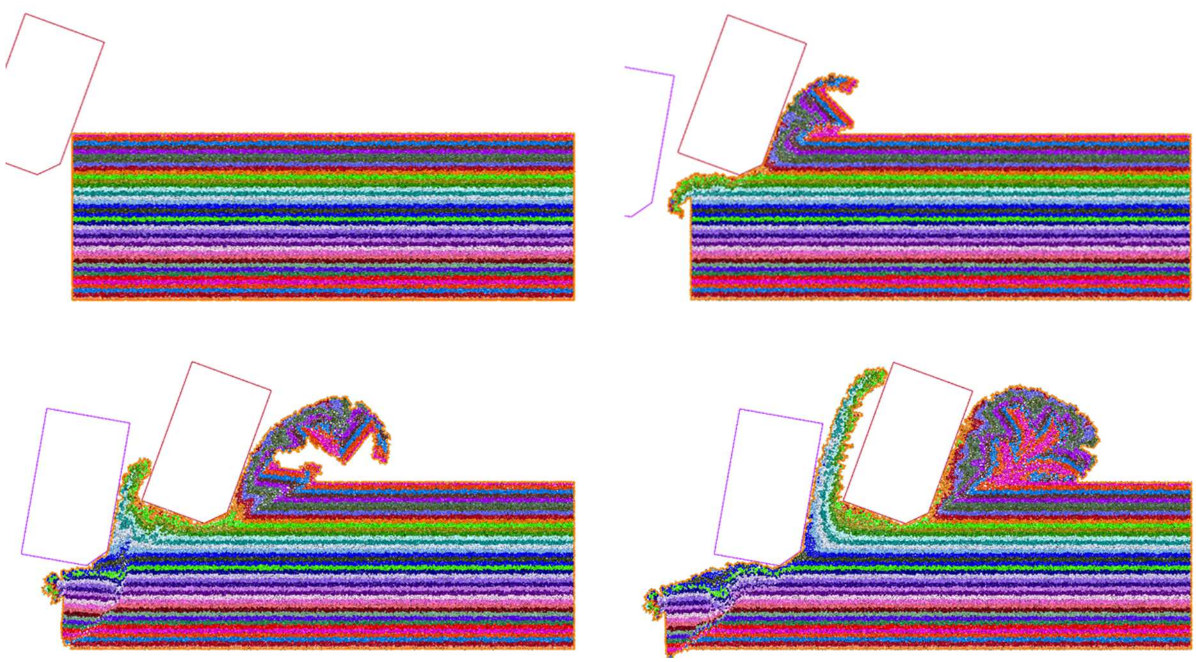

Figure 48 ***Material deformation during wet cutting of the TB50 material subjected to 1-MPa confinement for cutter-1 displacements of 0, 2, 4, and 6 mm.***

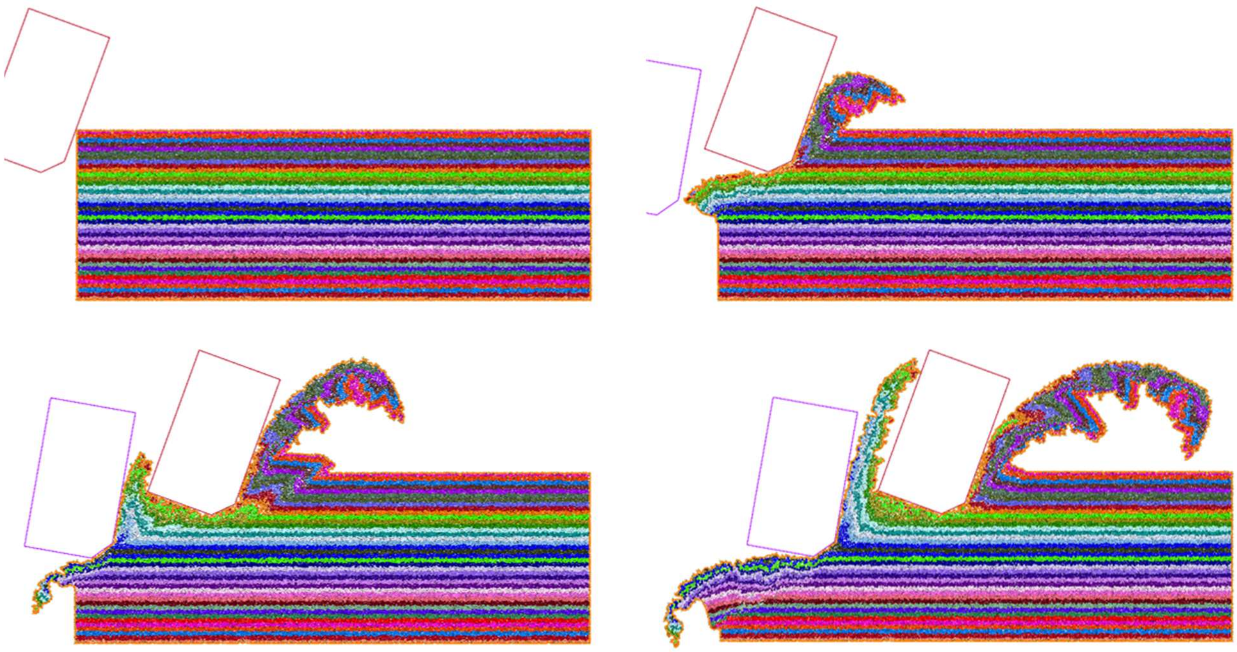

Figure 49 Material deformation during wet cutting of the TB50 material subjected to 5-MPa confinement for cutter-1 displacements of 0, 2, 4, and 6 mm.

Rahmani et al. (2016) suggest the following wet-cutting deformation mechanism (see Figure 50). Rahmani and coworkers state that

> the ductile failure of fine-grained, impermeable rocks such as shale under high confining pressure is thought to be similar to metal cutting . . . A phenomenon similar to cutter balling was described in metal cutting (Astakhov, 2006) as 'seizure,' which is when the temperature and contact pressure on the cutter/cuttings interface reach a certain level, the force required for the sliding of cuttings ribbon on the face of cutter (Path 1 in Figure 50) becomes greater than that required for plastic deformation of the cuttings being produced ahead of the partially formed ribbon. Therefore, as the cutter progresses, the cuttings feed into a growing mass at the bottom of the ribbon (Path 2 in Figure 50), leading to excessive deformation and compression of cuttings as they form.

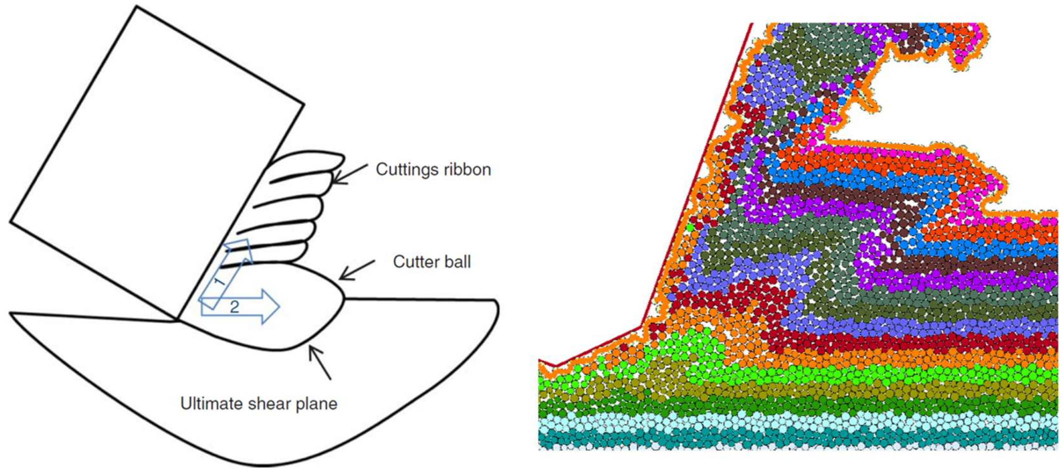

Figure 50 ***Sketch of postulated wet-cutting deformation mechanism (left), and deformation during wet cutting of the TB50 material subjected to 5-MPa confinement, showing horizontal layer being sheared off and then riding up the cutter face (right).*** (Left image from Fig. 12 of Rahmani et al. [2016])

The cutter forces for dry and wet cutting are shown in Figures 51 and 52. The forces during wet cutting at 5-MPa confinement are approximately an order of magnitude larger than during dry cutting. The wet-cutting forces are also more continuous than the dry-cutting forces. The wet-cutting forces remain greater than zero, whereas the dry-cutting forces consist of a near-zero value with a few large spikes. The more continuous nature of the wet-cutting forces demonstrates that the pressure application is causing the rock to remain in more intimate contact with the cutter than for the dry-cutting case. The wet-cutting forces exhibit fluctuations about non-zero values, which suggests an underlying brittle failure process along with a more ductile and continuous failure process.

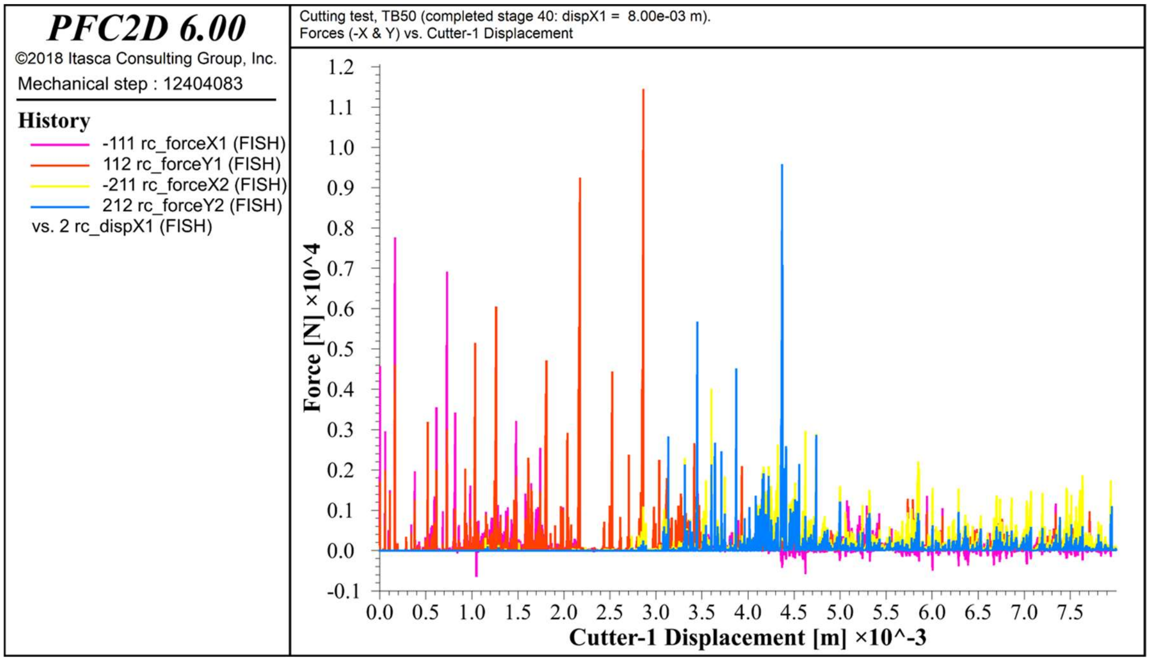

Figure 51 ***Cutter forces versus cutter-1 displacement during dry cutting of the TB50 material.***

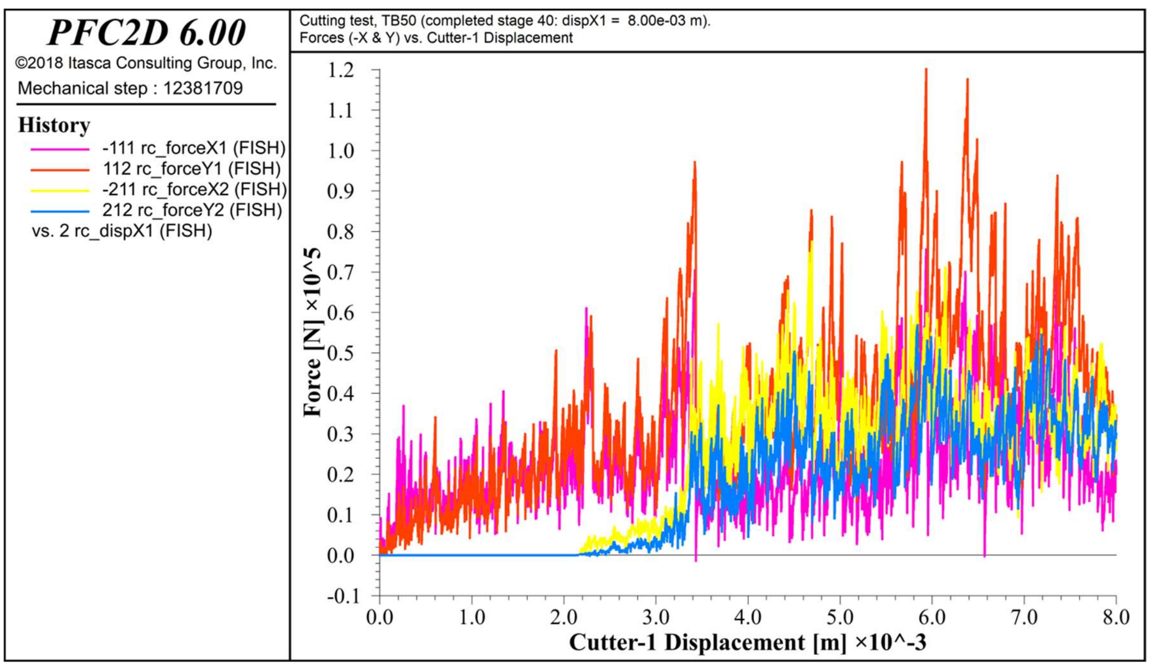

Figure 52 ***Cutter forces versus cutter-1 displacement during wet cutting of the TB50 material subjected to 5-MPa confinement.***

The damage and force-chain fabric in the near-cutter region during wet cutting is shown in Figures 53–55. The cutter is in contact with a mass of broken material (consisting of grains with all bonds broken) that is underlain by intact material with fingers of broken material extending downward away from the cutter. The broken material behaves like a loosely interlocked frictional granular material; it may be more realistic to make this material behave like a more interlocked sticky granular material.[22] This modified broken material may make the model's behavior more closely match what is believed to be the actual wet-cutting mechanism shown in Figure 50. The force-chain plots demonstrate that the cutter is loading the broken material, and the pressure is being applied to the mass of broken material that is moving up the cutter face. Providing a sealed region along the cutter keeps this material in intimate contact with the cutter, thereby inhibiting the formation of a gap at the cutter-rock interface and the associated forward bending of the material mass.

[22] Such a broken material is provided by the Adhesive Rolling Resistance Linear contact model. This model provides a frictional interaction with rolling resistance to which is added a cohesive component characterized by two parameters: maximum attractive force and attraction range. If this model for the broken material is adopted, then it may also be beneficial to replace the model for the intact material by switching from a parallel-bonded to a flat-jointed material. The flat-jointed material should allow one to match both the tensile and unconfined-compressive strengths of Torrey Buff sandstone — the parallel-bonded material matches the tensile strength but underestimates the unconfined-compressive strength. These material modifications are beyond the scope of the present project but should be considered for a subsequent project. LeBaron et al. (2024) have modeled rock cutting successfully using the PFC3D flat-jointed material. {Interest in rock cutting with PFC3D has been growing in SLB. We're up to 2 PFC licenses, 2 dedicated machines to run models, and trying to find another engineer to train as demand for my work has been steadily increasing. I've done many studies of cutter shapes, including some work analyzing/optimizing the Serra Blade cutting element. I credit the flat joint model for a lot of the success: It seems to capture the ductile-brittle transition in rock cutting, creating larger rock chips and lower specific energy at higher depths of cut. I also have indications that it matches fracture toughness for at least 2 rock types via laboratory rock chipping tests (not by any formal fracture toughness tests).}

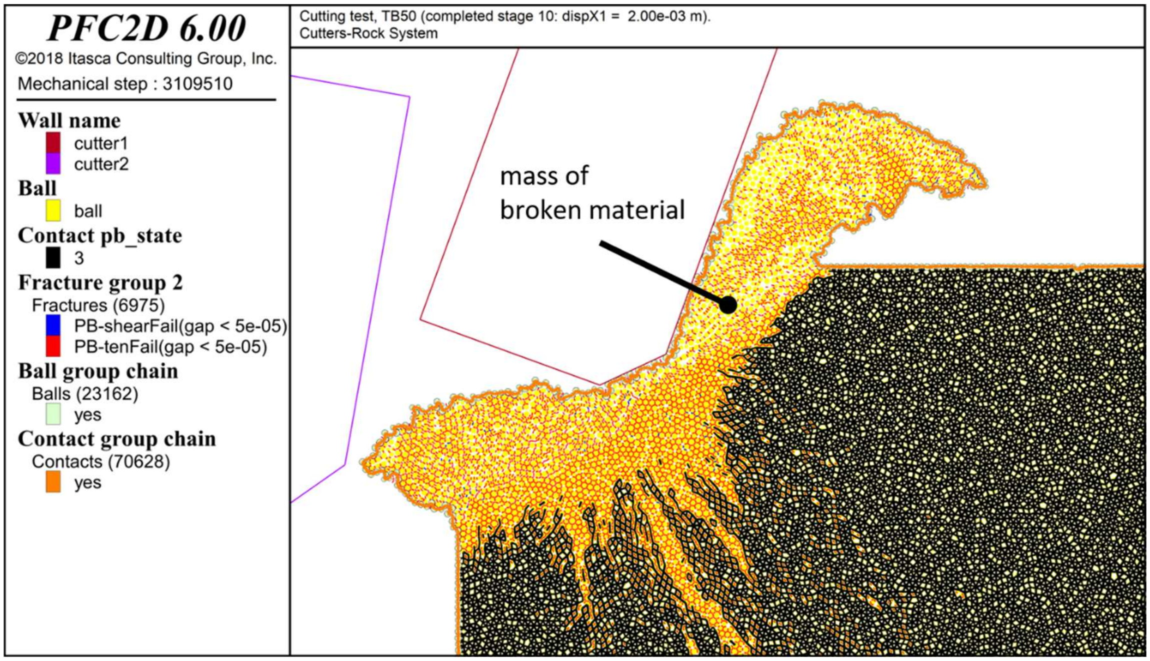

Figure 53 ***Damage during wet cutting of the TB50 material subjected to 5-MPa confinement for cutter-1 displacement of 2 mm.***

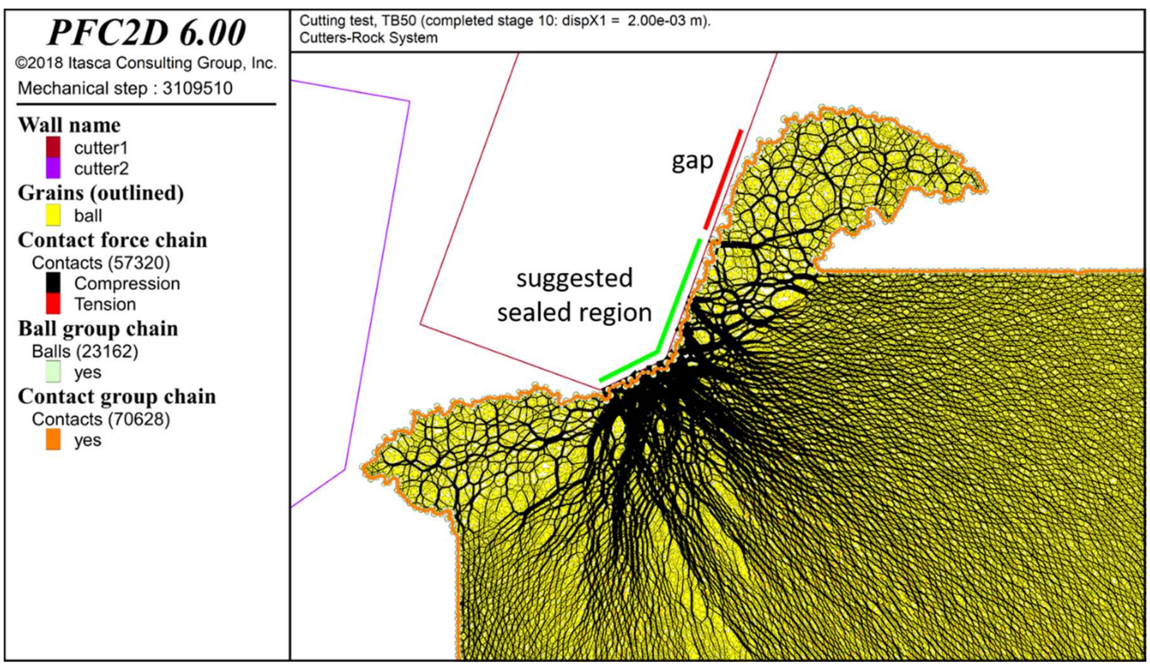

Figure 54 ***Force-chain fabric (bi-colored: compression and tension) during wet cutting of the TB50 material subjected to 5-MPa confinement for cutter-1 displacement of 2 mm.***

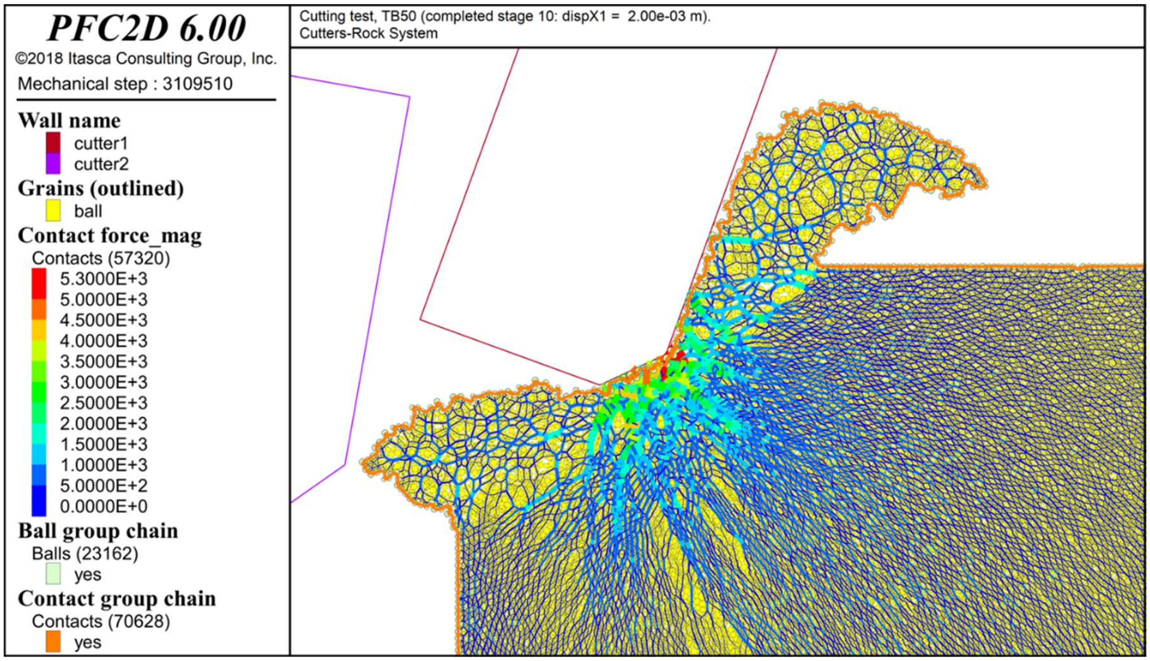

Figure 55 ***Force-chain fabric (scale colored: magnitude) during wet cutting of the TB50 material subjected to 5-MPa confinement for cutter-1 displacement of 2 mm.***

The energy quantities for dry and wet cutting are plotted versus cutting time in Figures 56 and 57. The energy required to cut 8 mm of rock under dry-cutting conditions is 1.7 J, whereas this energy increases to 348 J under wet-cutting at 5-MPa confinement. The energy consumed in slip under dry-cutting conditions is 58% of the total input energy, whereas the slip energy increases to 93% of the total input energy under wet-cutting at 5-MPa confinement. Most of the energy during wet cutting is consumed in slip, which corresponds with plastic deformation of the broken material as the grains slide past one another.

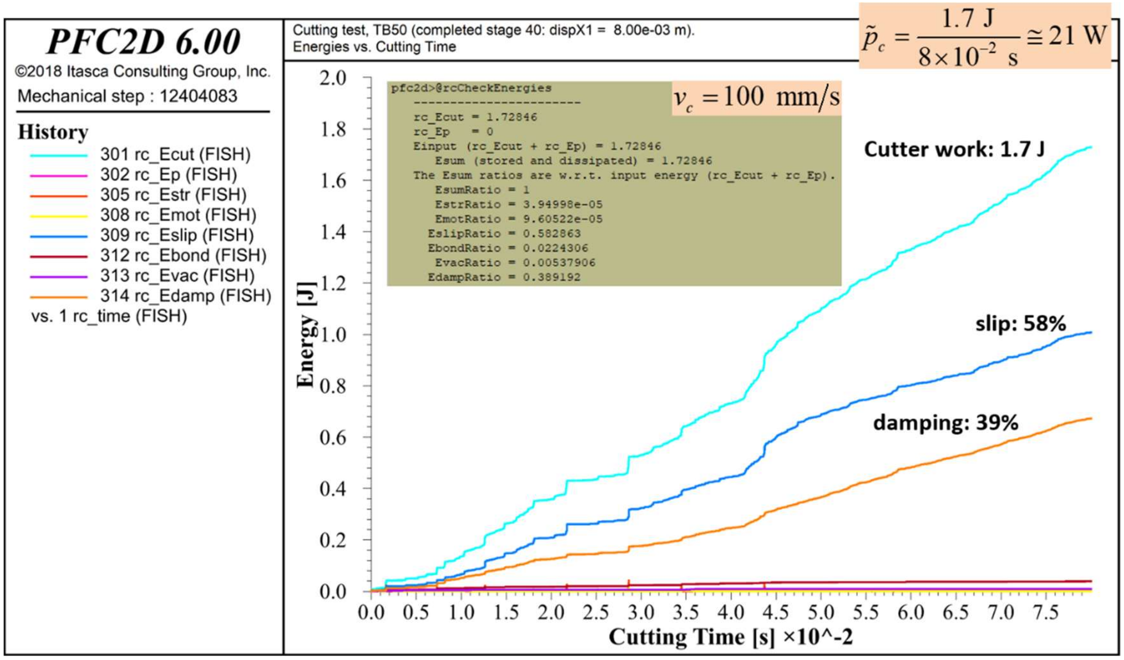

Figure 56 ***Energies versus cutting time during dry cutting of the TB50 material.***

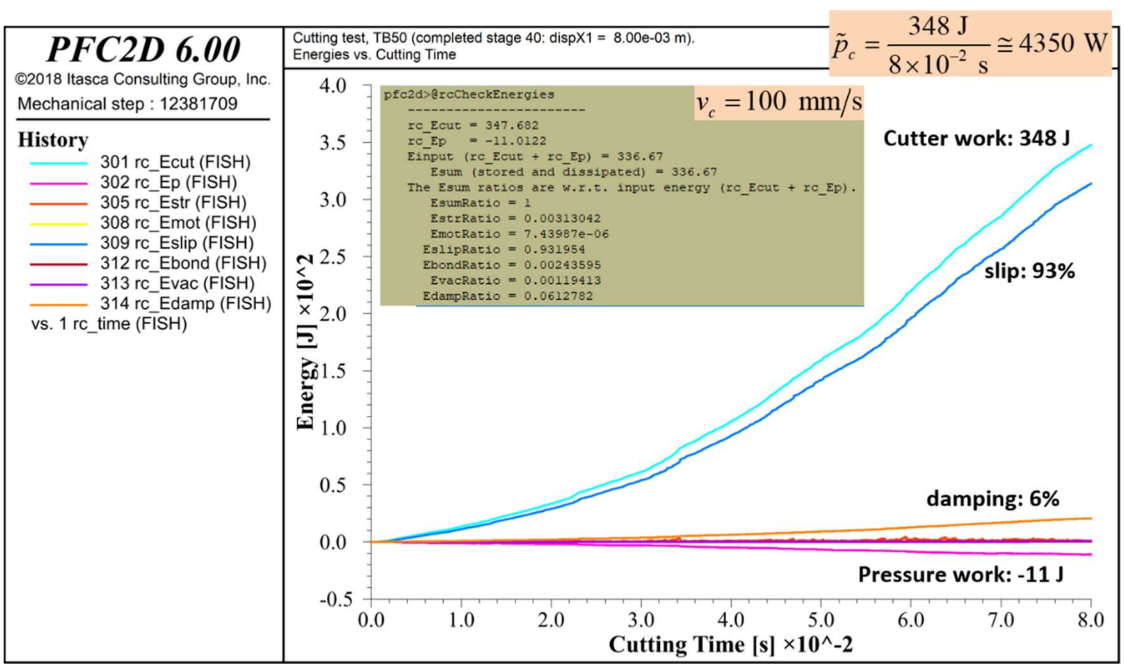

Figure 57 ***Energies versus cutting time during wet cutting of the TB50 material subjected to 5-MPa confinement.***

3.0 REFERENCES

Astakhov, V. P. (2006). *Tribology of Metal Cutting, Volume 52* (1st ed.). Elsevier.

Blanksma, D., & Potyondy, D. (2015). PFC rock-cutting model (physical data for Torrey Buff sandstone). Itasca Consulting Group, Inc., Technical Memorandum ICG15-2911-33TM (May 21, 2015). **TM-PhysicalData_TB.pdf**

Cumulative moving average. (2026, July 20). In *Wikipedia*.
https://en.wikipedia.org/wiki/Moving_average#Cumulative_average

ITASCA. (2026a). PFC Suite — Particle Flow Code in Two and Three Dimensions (Version 9.0). Itasca Consulting Group, Inc.
https://www.itascainternational.com/software/pfc
https://docs.itascasoftware.com/itasca970/pfc/docproject/source/manual/pfchome.html

ITASCA. (2026b). FLAC3D — Fast Lagrangian Analysis of Continua in Three-Dimensions (Version 9.0). Itasca Consulting Group, Inc. Maxwell damping is described at
https://docs.itascasoftware.com/itasca970/flac3d/docproject/source/options/dynamic/damping/damping.html?node3964#maxwell-damping

LeBaron, A., Gan, X., McLennan, J., Marquardt, J., Belnap, D., & Fang, Y. (2024). High temperature characterization and drilling simulation of rock from Utah FORGE. In *Proceedings, Geothermal Rising Conference, GRC 2024*, *GRC Transactions, 48*.
LeBaronEtal(2024)-PFC3Drockcut.pdf

Ledgerwood, L. W. (2013). PFC3D modeling of rock cutting under pressure calibrated to the inelastic region of triaxial tests at high strain. In *Proceedings, 6th International Conference on Discrete Element Methods, DEM6 (Colorado, USA, August 5-6, 2013)*. **Ledgerwood(2013)-PFC3D_RockCutting.pdf**

Ledgerwood, L. W. (2012). Discrete element modeling of rock destruction under high pressure conditions. United States Patent No. US 8,150,667 B2 (April 3, 2012).

Newman, W. M., & Sproull, R. F. (1979). *Principles of Interactive Computer Graphics* (2nd ed.). McGraw-Hill Book Company.

Potyondy, D. (2026). Sandstone package for PFC2D and PFC3D [ssPkg9.6b]. Itasca Consulting Group, Inc., Technical Memorandum 2-6867-02:25TMxx (April 11, 2026).

Potyondy, D. (2025). Material-modeling support for PFC [fistPkg9.3]. Itasca Consulting Group, Inc., Technical Memorandum ICG7766-L (April 24, 2025).
https://www.itascacg.com/software/material-modeling-support

Potyondy, D. (2019a). Rock-cutting package for PFC2D [rcPkg6.4]. Itasca Consulting Group, Inc., Technical Memorandum 2-5265-01:19TM13 (March 5, 2019). **RockCuttingPkg[6.4].pdf**

Potyondy, D. (2019b). Micromechanical spalling model (material calibration). Itasca Consulting Group, Inc., Technical Memorandum 2-5732-01:19TM17 (April 19, 2019). In Micromechanical spalling model. Itasca Consulting Group, Inc., Report to Svensk Kärnbränslehantering AB (SKB), Stockholm, Sweden, 2-5732-01:19R16, April 19, 2019.

Potyondy, D. O. (2015). The bonded-particle model as a tool for rock mechanics research and application: current trends and future directions. *Geosystem Engineering, 18*(1), 1–28. https://doi.org/10.1080/12269328.2014.998346

Potyondy, D. (2012). PFC3D pressure boundary condition. Itasca Consulting Group, Inc., Technical Memorandum ICG7233-L (January 30, 2012).

Potyondy, D. O., & Cundall, P. A. (2004). A bonded-particle model for rock. *Int. J. Rock Mech. & Min. Sci.*, *41*(8), 1329–1364. https://doi.org/10.1016/j.ijrmms.2004.09.011

Potyondy, D., & Blanksma, D. (2015). PFC rock-cutting model — Phase 1: Dry cutting. Itasca Consulting Group, Inc., Report to National Oilwell Varco (NOV), Houston, Texas, ICG15-2911-18, May 21, 2015. **RockCuttingModel-Phase1.pdf**

Rahmani, R., Ferrel, R. E., & Smith, J. R. (2016). Multiscale imaging of fixed-cutter-drill-bit-generated shale cuttings. *SPE Reservoir Evaluation and Engineering*, *19*(2), May 2016, paper SPE 176028, doi:10.2118/176028-PA.

Schöpfer, M. P. J., Childs, C., Manzocchi, T., & Walsh, J. J. (2017). Three-dimensional distinct element method modelling of the growth of normal faults in layered sequences. *Geological Society, London, Special Publications, 439*, 307–332. https://doi.org/10.1144/sp439.17